Schweizerischer Erdbebendienst
Service Sismologique Suisse
Servizio Sismico Svizzero
Swiss Seismological Service

ETH zürich

SITE CHARACTERIZATION REPORT

STSW2: Lac de Zeuzier (VS) - Stausee

Paolo Bergamo, Manuel Hobiger, Donat Fäh

Last Modification: 21st December, 2017

Schweizerischer Erdbebendienst (SED)
Service Sismologique Suisse
Servizio Sismico Svizzero
Servizi da Terratrembels Svizzer

ETH Zürich
Sonneggstrasse 5
8092 Zürich
Schweiz
paolo.bergamo@sed.ethz.ch

Contents

1 Summary

The SSMNet station STSW2 was installed close to the artificial dam on the south-east shore of the Lac de Zeuzier reservoir, in the territory of the municipality of Ayent (VS). Active seismic measurements, as well as several noise recording surveys, were conducted prior to the station installation, with the aim of characterizing the area of interest (i.e. the south-east shore of the lake) and determining the most appropriate location for the SSMNet station. The targeted area is a sedimentary rock ridge closing a mountain basin, divided in its central section by a cleavage sealed by an artificial arch dam of 156 m height (Zeuzier Dam), and an earthfill dam of 20 m height to the west (Proz-Riond Dam). Two active seismic lines were deployed on the ridge at both sides of the Zeuzier dam. The retrieved velocity profiles (site class A) identify about 5 m of soil cover, overlying 15 to 20 m of degraded rock, in turn resting on a fresh rock bedrock. The two interfaces correspond to peaks at 23 to 32 Hz and around 16 Hz in the H/V curves derived from the passive recordings acquired on the rock formation. These are also characterized by fundamental peaks at much lower frequencies (around 4 Hz), that can be explained with an interface within the rock formation, at larger depths than those surveyed by active acquisitions. The south-west shoulder of the ridge is covered by debris. This area was investigated with one active seismic line; the obtained velocity models place the interface between the shallower debris sediments and weathered rock at a depth of around 20 m. This boundary can be correlated with the fundamental frequency peaks (6 to 8 Hz) observed in the H/V curves from passive recordings performed in the debris fan area. The soil classification at this site is at the border between class B and E. The station STSW2 was eventually installed at a location not directly covered by active or passive measurements. Therefore, a proper and robust estimation of the seismic properties of the subsurface just below the SSMNet station could not be achieved; nevertheless, it is possible to propose a plausible subsoil profile.

2 Introduction

In the framework of the second phase of the SSMNet (Swiss Strong Motion Network) renewal project, station STSW of the old strong motion network was planned to be renewed. STSW was located inside a tunnel (about 5 m from the tunnel entrance) in the mountains to the west of the Lac de Zeuzier. The new station STSW2 was installed on 16 August 2016 in vicinity of the artificial dam on the south-eastern shore of the Lac de Zeuzier, in the municipality of Ayent (VS), at an altitude of 1774 m above sea level (Fig. 1). Before the installation of the station, seismic measurements were carried out on 2 July 2015 in the area of interest with the aim of determining the seismic properties of the site and identifying the most suitable location for STSW2. The peculiar morphology of the site (a ridge marking the border of an artificial lake, in turn nested in a narrow mountain basin) makes it unsuitable for the execution of array-based passive noise recordings, involving circular or circular-like deployment schemes. Considering also the expected shallow depth of the bedrock at the site, active seismic surveys and several single-station H/V measurements were carried out to ensure the seismic characterization of the area.

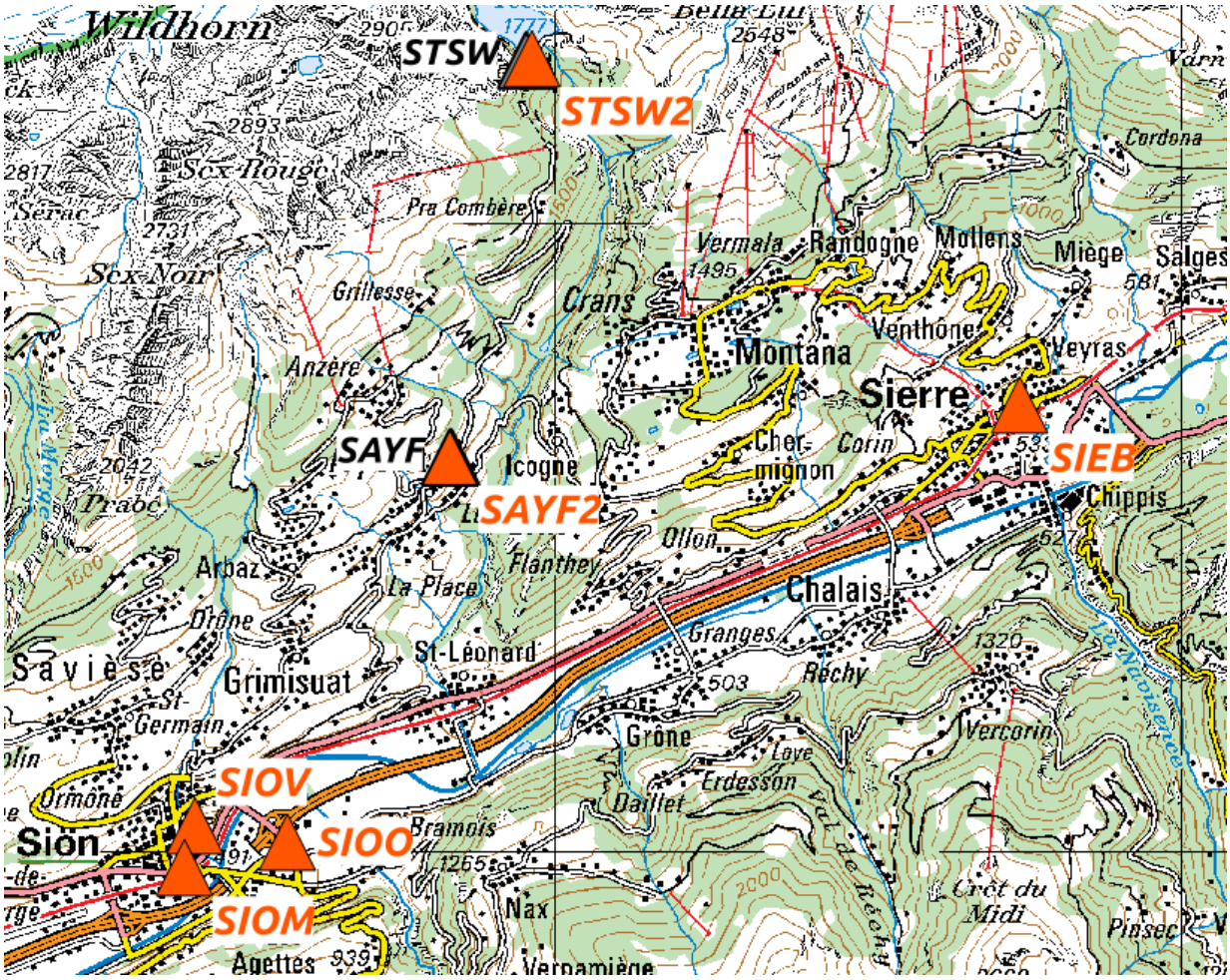

Figure 1: Location of station STSW2 in the Valais. Active SSMNet stations are shown as orange triangles, old stations in black. ©2017 swisstopo (JD100042).

3 Geological setting

The site is located on a rocky ridge marking the south-eastern shore of the Lac de Zeuzier. In its central section, the ridge opens in a v-shaped cleavage, bridged by Zeuzier Dam, an artificial dam of 256 m length and 156 m height. To the west of the station location, an earthfill dam of 20 m height (Proz-Riond Dam) blocks another smaller cleavage. According to available geological information, the rock formation is made up of limestone, and it is cut by faults in its central part (beneath the dam) and on the north-east and south-west extremities (Fig. 2). The south-west end of the ridge, close to STSW2, is occupied by debris arranged in dry alluvial fans.

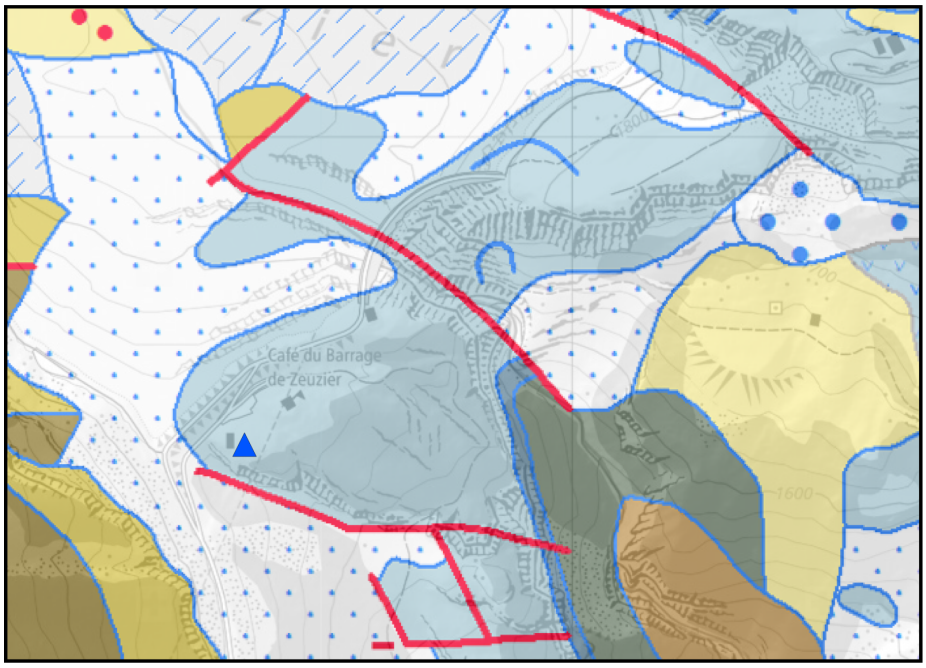

Figure 2: Geological map of the of the surroundings of STSW2 (blue triangle). The pale blue area, where the station is located, corresponds to limestone of the Séquanien-Portlandien, the white area with blue dots to debris, the ocher area in the southwest and north to Hauterivien, the brown area in the southwest to Valanginien schisteux. ©2017 swisstopo (JD100042).

4 Active seismic measurements

The geomorphological configuration of the targeted area is not suitable for the application of array noise recording techniques. Furthermore, the surveyed zone is known to be characterized by a shallow bedrock; both features suggested the use of active seismic techniques. Three seismic lines, constituted by three-component (3C) geophones, were placed at three locations considered representative of the targeted area and also at the time of measurement as possible locations for the installation of the permanent station (Fig. 3):

- The first line, hereinafter referred to as "Tseu1", was deployed close to the south-west corner of the Lac de Zeuzier.
- The second line, "Tseu2", was placed on the rock formation to the north-east of the Zeuzier Dam.
- The third line, "Tseu3", was deployed on the rock formation to the south-west of the Zeuzier Dam, i.e. between the Zeuzier and the Proz-Riond Dam.

For the sake of a comprehensive subsurface seismic characterization, acquired data were interpreted with the application of both multichannel analysis of surface waves (MASW; Park et al., 1999) and P-wave refraction (Redpath, 1973) techniques.

4.1 Equipment

For all active lines, 3C 4.5 Hz geophones were used as receivers, coupled with the ground by means of metal spikes penetrating the subsoil. Arrays Tseu1 and Tseu2 were constituted by three sets of 8 geophones each, for a total of 24 receivers. Array Tseu3 was made up of two sets of 8 receivers. Each geophone set was connected to a Geode datalogger; Geodes belonging to the same line were coupled for time synchronization. The employed seismic source was a 5 kg sledgehammer hitting a flat metal plate placed on the ground. The synchronization between the recorded traces and the seismic source was ensured by a trigger device firmly fastened to the hammer handle.

4.2 Geometry of the acquisition arrays

Lines Tseu1 and Tseu2 were constituted by 24 three-component receivers, arranged in a linear spread with an inter-geophone distance of 1 m (length of the line 23 m). Tseu3 consisted of 16 three-component receivers, deployed with a regular spacing of 1 m (length of the line 15 m). For all arrays, the seismic sources were positioned at several locations along the line defined by the receivers. At both ends of the lines, the sources were placed at 1, 5 and 10 m (9 m for Tseu3) offsets from the outermost sensors (see Fig. 4).
Seismic traces recorded with shooting points at 1 m from the geophone arrays were used for refraction analysis; seismograms with shooting points at 5 m from the array were exploited for MASW technique, as 5 m was considered a distance long enough to avoid near-offset effects (Socco and Strobbia, 2004). [Socco and Strobbia, 2004] The coordinates of the source and receiver positions were determined on site with a differential GPS.

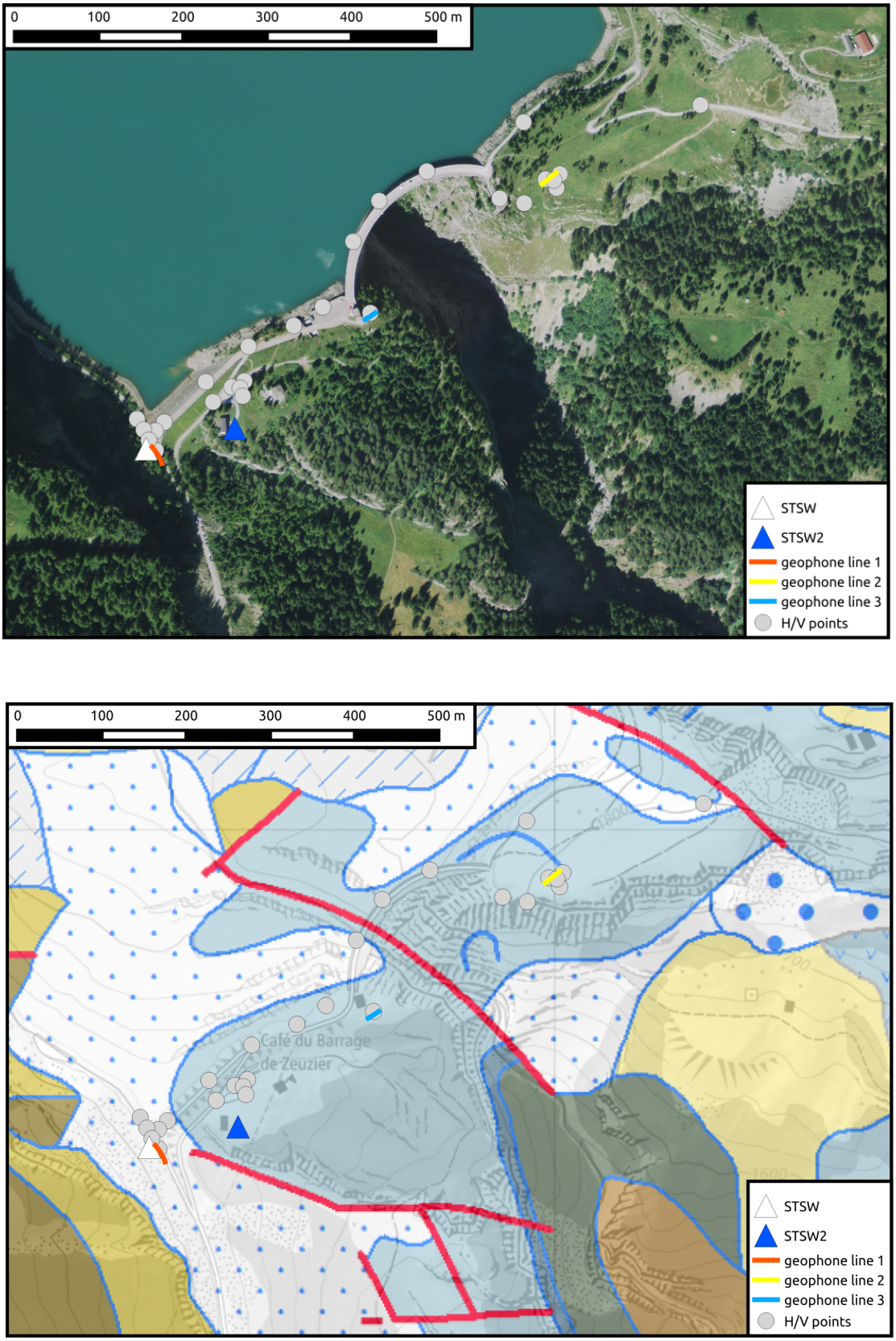

Figure 3: Maps representing the locations of the three active seismic arrays, the positions of the single-station noise recordings and station STSW2. Top: Aerial map. Bottom: Geological map (see Fig. 2 for the legend). ©2017 swisstopo (JD100042).

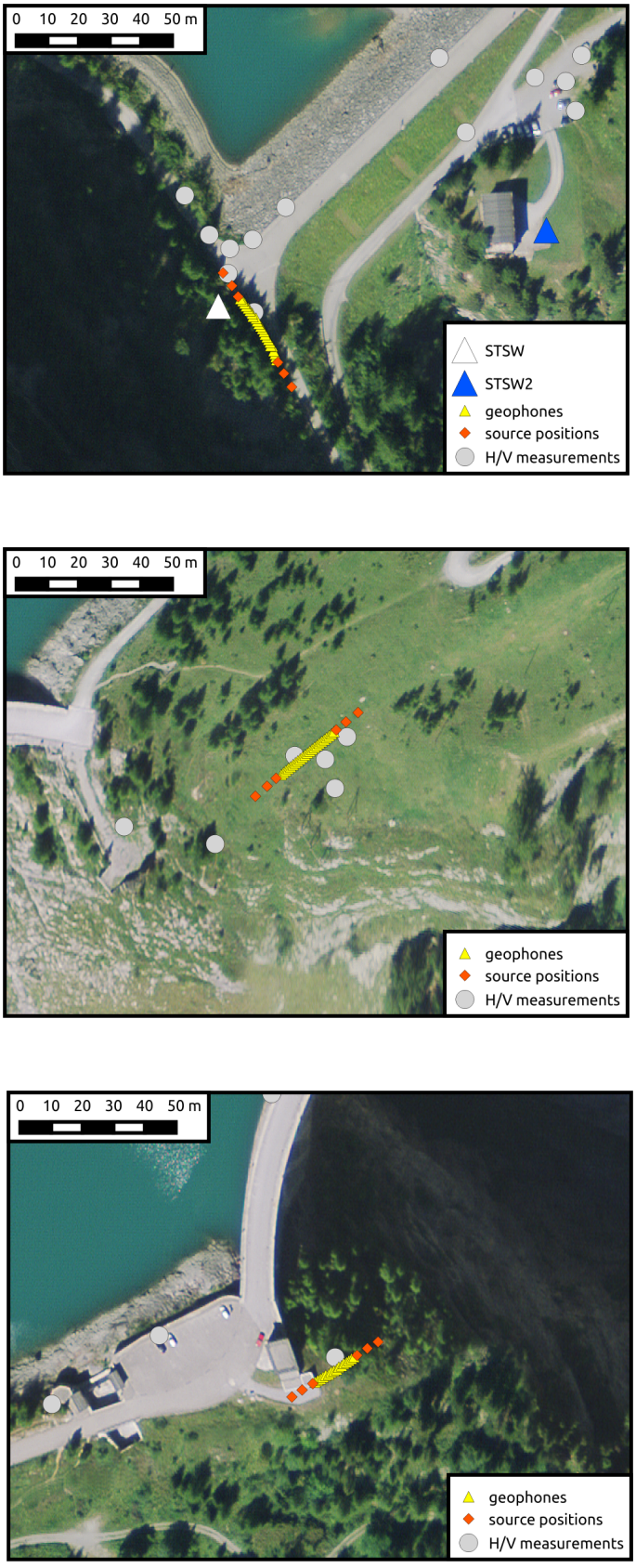

Figure 4: Geometry maps of the active seismic arrays Tseu1, Tseu2 and Tseu3 (from top to bottom. ©2017 swisstopo (JD100042).

4.3 Acquisition

The time sampling parameters adopted for Tseu1, Tseu2 and Tseu3 were the following: sampling interval = $1.25 \cdot 10^4\, s$, record length = $0.5\, s$, pre-trigger delay = $0\, s$. At each source point, 10 hammer blows were successively shot; at each shot, the recordings from all geophones were saved in a separate .sg2 file. Fig. 5 represents a sample seismic section from Tseu2. As three-component geophones were used, three traces are available for each receiver: one corresponding to the vertical component of vibration of the soil surface and two corresponding to the two components, mutually orthogonal, of horizontal displacement (Horizontal 1 = longitudinal with respect to the receiver array; Horizontal 2: transversal with respect to the receiver array).

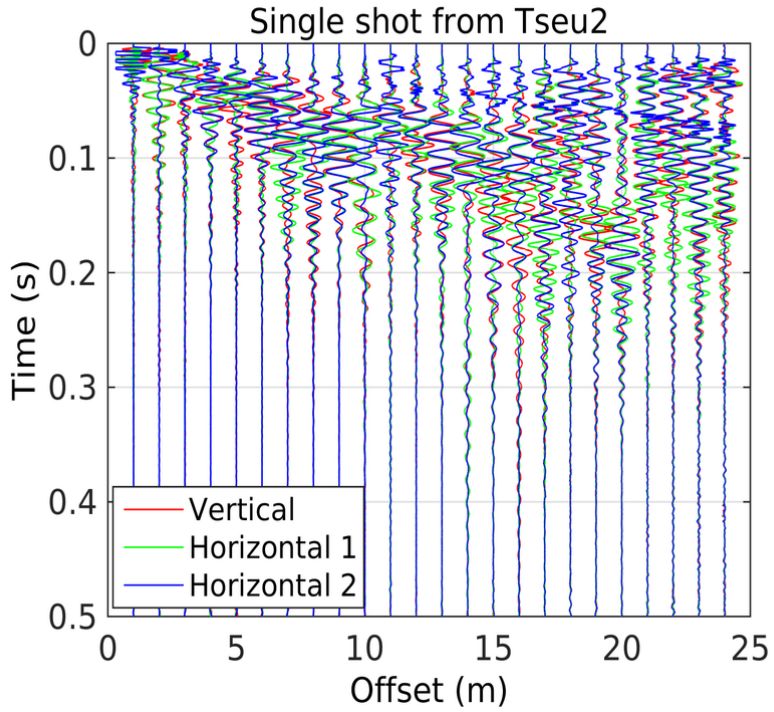

Figure 5: Sample seismic sections (vertical and horizontal components) for a shot from Tseu2.

4.4 Processing

4.4.1 Preprocessing

The seismic traces generated by the different shots with the same source location were summed - or stacked - in time domain. This operation is enhancing the coherent seismic events generated by the controlled seismic source (sledgehammer blow) and at the same time minimizing the uncoherent noise present in the recordings (Foti et al., 2015). "Stacked" seismic sections, with greater signal-to-noise ratio, were hence obtained (Fig. 6). To preserve the effectiveness of the stacking operation, the seismic traces of the vertical component at shortest offset were cross-correlated to ensure an adequate synchronization among the seismograms to be later superimposed (Fig. 7). The small shifts that are evident in the top panel of Fig. 7 can be ascribed to a non-ideal behavior of the trigger device, or to small movements of the metal plate from one shot to the successive one

caused by the hammer blow and the subsequent “bouncing” of the plate on the hard ground.

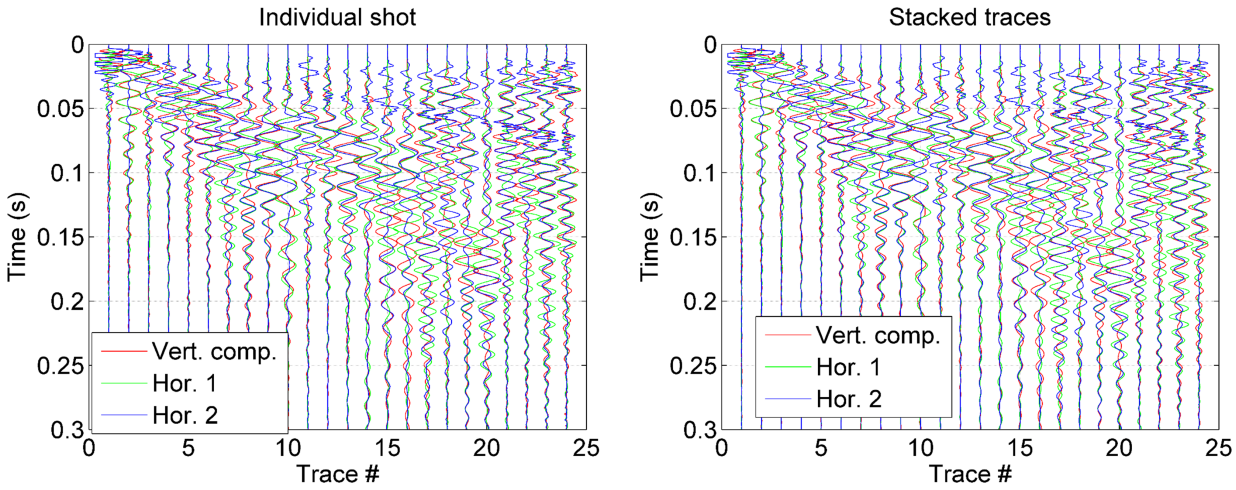

Figure 6: Single shot seismograms (left) and "stacked" seismic sections (right) obtained by summing the 10 sets of traces acquired with the same source-receiver configuration.

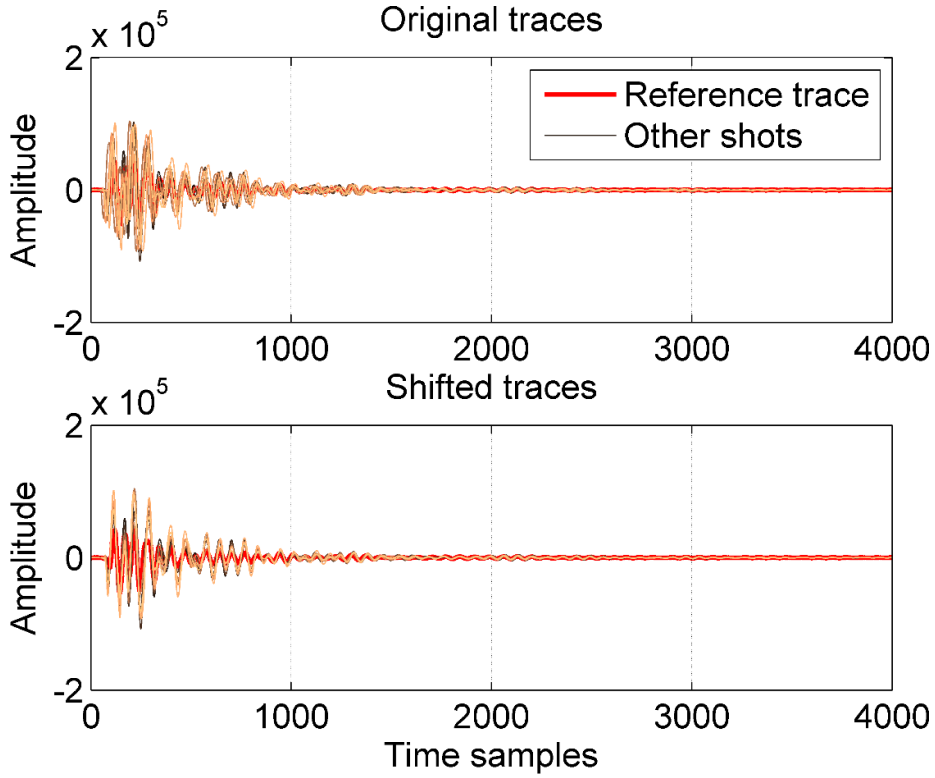

Figure 7: Retrieving the optimal synchronization among seismic traces before stacking. Top: Nearest offset seismic traces (vertical component) recorded at 10 different shots acquired with the same source-receiver configuration (Tseu2). Bottom: Synchronized traces after the shifts for an optimal synchronization were retrieved via cross-correlation.

4.4.2 P-wave refraction processing

P-wave first break arrival times were manually picked on the stacked seismograms representing the vertical component of soil surface vibration, from the suitable shooting-recording configurations (source placed at 1 m offset from the array at both ends: see Fig. 8 for an example). The identification of P-wave arrival times was particularly cumbersome at all three sites, possibly because of a non-ideal receiver-soil coupling (expected in very stiff soils). The interpretation of the retrieved hodocrones, with the intercept time technique (Reynolds, 2011) was challenging as well: as shown for instance in Fig. 8b, the travel time curves from direct and reverse shots often presented inconsistent arrivals, suggesting an irregular surface for the shallow bedrock interface. The model obtained for Tseu2 can be considered realistic: consistently with the field observations, two layers of surficial soil cover, with increasing stiffness (0.9 m thick, $V_P = 695\,m/s$; 3.7 m thick, $V_P = 1094\,m/s$), overlie the bedrock ($V_P = 3657\,m/s$, at 4.5 m depth). For Tseu1 and Tseu3, the identification of the bedrock upper boundary at depths of 0.8 to 1.8 m is unrealistic (particularly for Tseu1, where the seismic line was placed in the area covered by debris alluvial fans, hence the deepest refractor depth should be larger than in Tseu2). The unreliability of the estimated profiles can be explained, at least for Tseu1, with the presence of a containment wall vertically embedded in the soil very close to the receivers' array: most likely, the identified refracted arrivals are to be ascribed to the concrete wall, rather than to the bedrock.

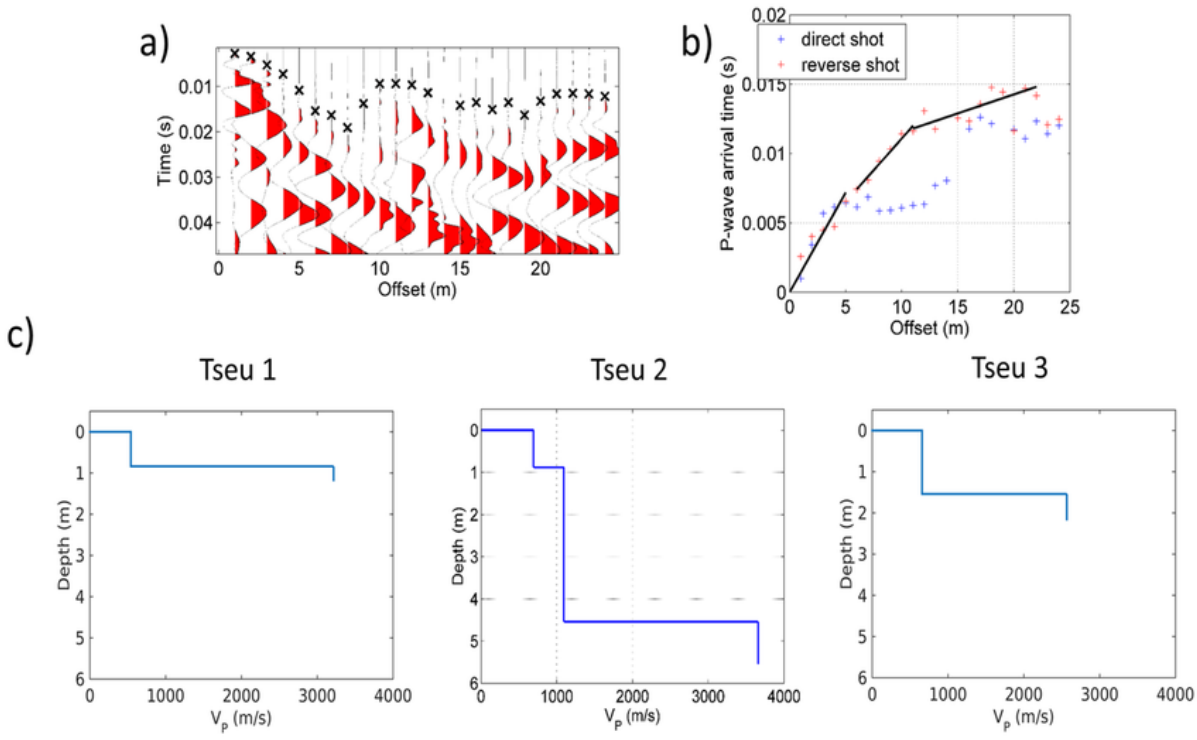

Figure 8: Processing and interpretation of P-wave refraction data. a) Picking of first-break P-wave arrival times frm a sample seismic section (Tseu2). b) Intercept time interpretation of arrival times (Tseu2). c) Obtained shallow V_P profiles for the three sites.

4.4.3 MASW processing

Vertical and longitudinal component seismograms from MASW acquisitions, considering both single shot and stacked seismic sections, were processed by means of a 2D f-k (frequency – wavenumber) transform (Socco and Strobbia, 2004) to obtain a conversion of the recorded sets of traces from time–offset to frequency–wavenumber domain. The energy maxima in the retrieved f-k panels correspond to the propagation of Rayleigh waves and they depict the Rayleigh waves' dispersive behavior (Socco and Strobbia, 2004; Foti et al., 2015). The maxima in the f-k panels from stacked seismic sections were picked by manually defining regions of interest in the f-k domain and then automatically identifying the peaks, frequency by frequency, within the selected areas (Fig. 9). The defined regions of interest were also automatically applied to the f-k spectra from single shot seismograms.
For each recording array (Tseu1, Tseu2, Tseu3) and for each considered component (vertical or longitudinal) we obtained:

- Two sets of f-k maxima (one for each source point in off-end configuration), retrieved from the stacked seismic section, that define the corresponding dispersion curve (red and blue, cyan and magenta dots in Fig. 10).
- Ten sets of f-k maxima, each of them derived from a single shot seismogram, that define the experimental uncertainty for the dispersion curve introduced in the first step (orange colored dots in Fig. 10).

This processing procedure follows the scheme described by Socco et al. (2009) and Boiero and Socco (2010).
The identified Rayleigh wave dispersion curves in Fig. 10 are composed of several phase velocity–frequency branches, arising from f-k panels which are complex and include several events, extending for limited frequency bands, none of them dominating (Fig. 9). Nonetheless, one can observe some consistency among the dispersion images obtained for the same array but considering different shooting configurations and recorded components. The presence of various dispersive events, of difficult identification (i.e. mode numbering), is to be ascribed to the shallow bedrock depth that determines the repartition of the source energy over several modes without predominantly following the fundamental mode (as in the case of a normally-dispersive subsurface: Foti, 2002; Maraschini and Foti, 2010).
Finally, it is significant to observe that the phase velocities retrieved for Tseu1 are generally lower than those from Tseu2 and Tseu3. This is consistent with the geological description of the three sites. Tseu2 and Tseu3 are directly located on the rock formation, while array Tseu1 was deployed in the area occupied by debris.

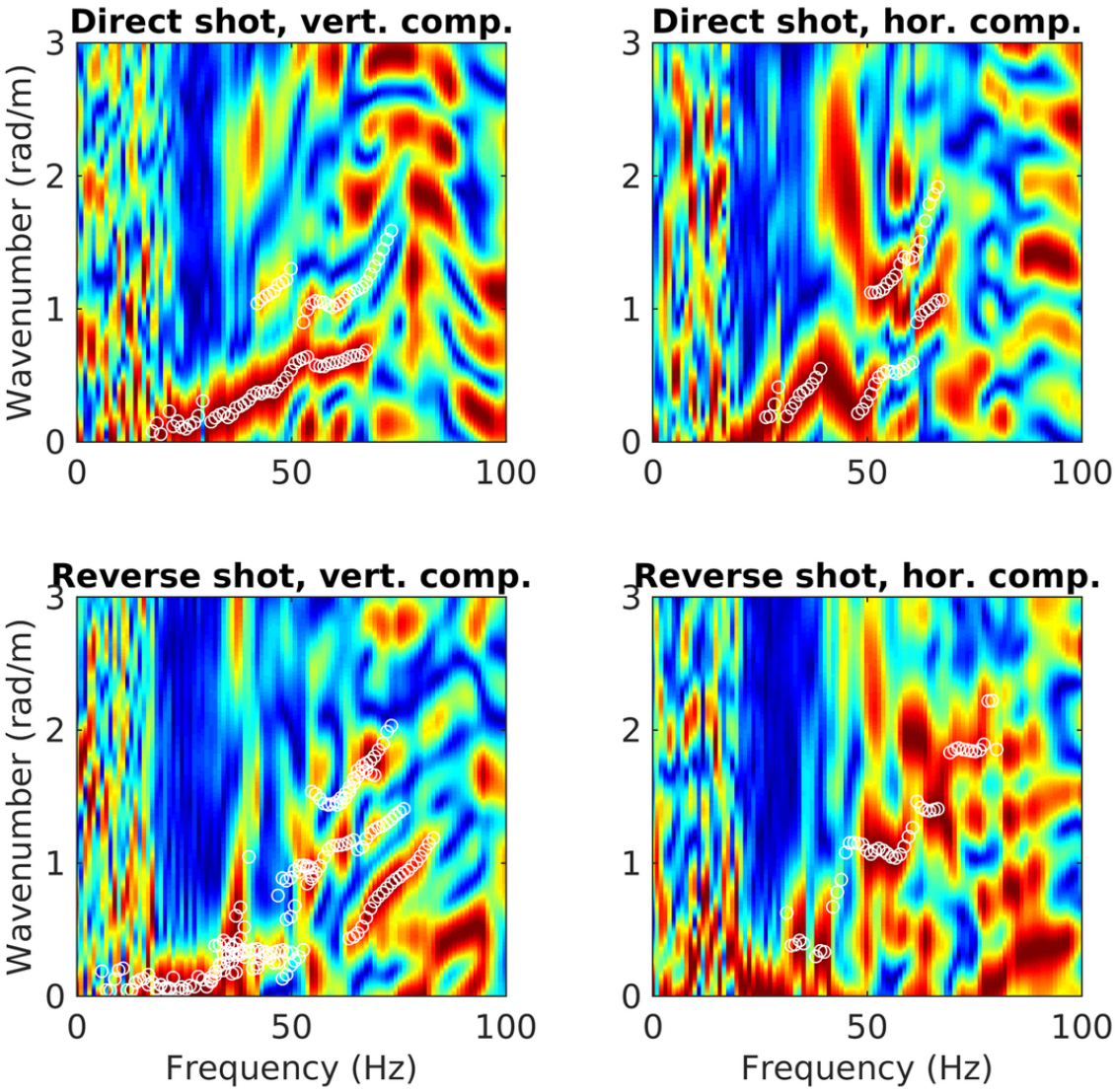

Figure 9: Normalized f-k spectra obtained from vertical and longitudinal components of stacked seismic sections of MASW recording configurations (Tseu2). Picked energy maxima are represented as white circles.

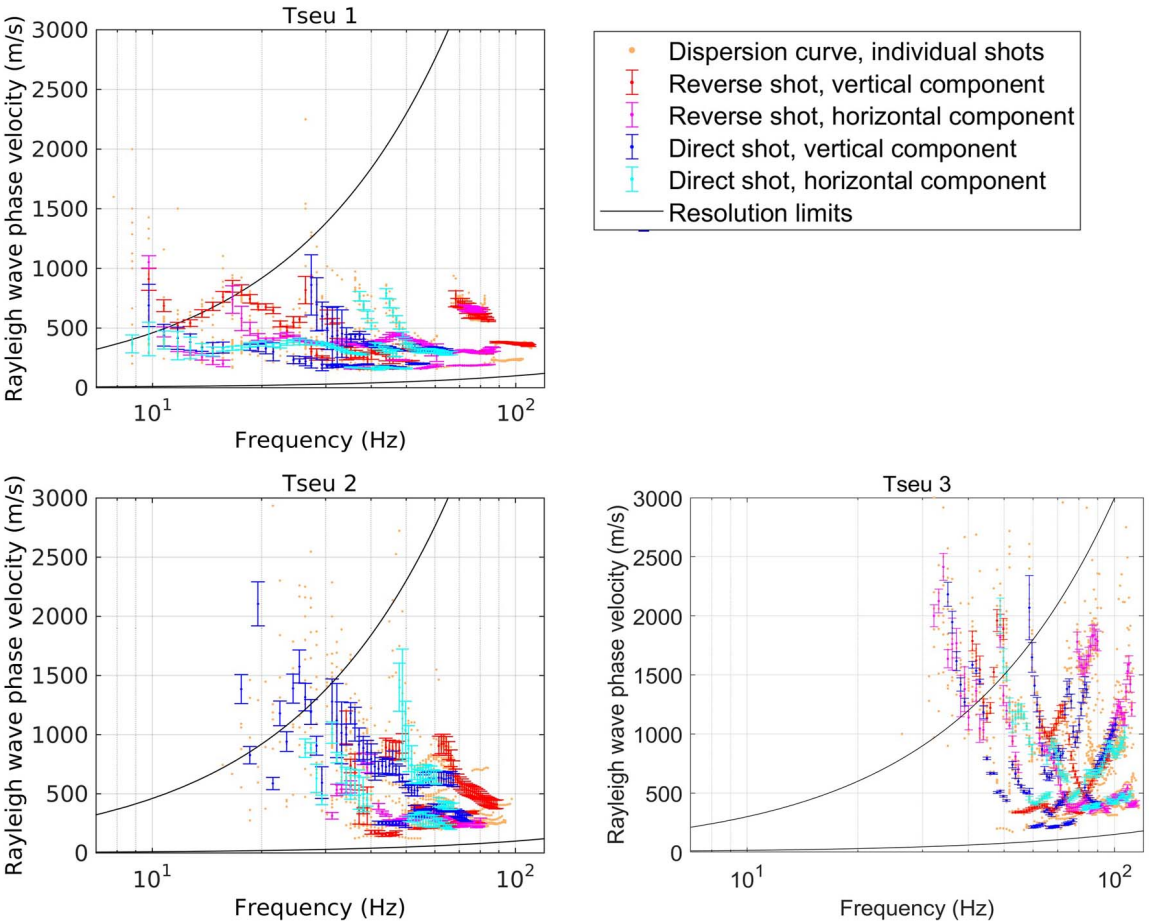

Figure 10: Obtained Rayleigh wave dispersion curves from the three arrays (Tseu1, Tseu2, Tseu3).

4.4.4 WaveDecActive

3C active recordings acquired by lines Tseu1, Tseu2 and Tseu3 were also processed with the WaveDecActive code (Maranò et al., 2017). WaveDecActive implements a maximum likelihood algorithm for the analysis of Rayleigh waves generated by a controlled source. Differently from the more conventional f-k analysis approach (4.4.3), it is able to characterize the Rayleigh wave propagation in terms of both phase velocity and ellipticity angle. The maximum number of Rayleigh waves that the code attempts to identify can be fixed. Furthermore, by changing the parameter γ the modeling can be switched from identifying Rayleigh waves by a purely Bayesian information criterion ($\gamma = 1$) to a pure maximum likelihood approach ($\gamma = 0$), or a compromise between the two ($0 < \gamma < 1$). Following the recommendations of the code's author for active data processing, the maximum number of waves was set to 5 and γ to 0.1, thus opting for a more aggressive approach, close to a pure maximum likelihood criterion. Examples of obtained processing results are displayed in Fig. 11.
Similarly to what had been previously observed (4.4.3), the obtained dispersion images are characterized by several scattered events of unclear mode identification. This means that also an advanced method such as WaveDecActive, based on the recognition of Rayleigh wave propagation (and not simply on raw identification of energy distribution, as f-k processing), cannot reconstruct a clear dispersion pattern in presence of a complex energy repartition, as that induced by a shallow stiff interface.
As the WaveDecActive results do not seem to provide clearer information, they are not included in the subsequent inversion process (section 6).

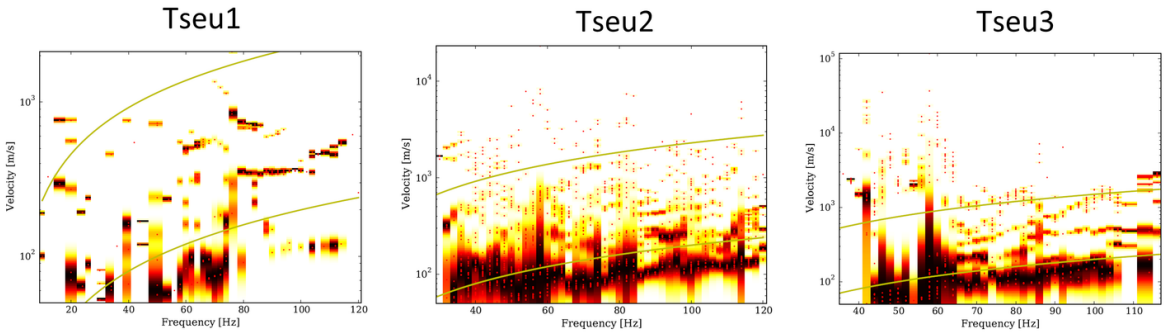

Figure 11: WaveDecActive processing results. Estimated Rayleigh wave phase velocities from the 3C seismic traces recorded by Tseu1, Tseu2 and Tseu3. Estimated phase velocity values are represented as red dots, whose density in the distribution across the velocity/frequency panel corresponds to the shaded colors. Golden lines define the array resolution limits as defined in the WaveDecActive code.

5 Passive seismic measurements

We performed an extensive survey of passive seismic measurements on the different parts of the area, including on top of the dams. Lennartz 5s seismometers were deployed at a total of 28 measuring points (see Fig. 12). At each of these points, passive seismic noise has been measured for at least one hour. At each point, the recordings were analyzed with single-station methods like H/V and the polarization analysis (Burjánek et al., 2010, 2012). In addition, at some places the sensors were deployed as small arrays consisting of four or seven sensors. The first of these arrays, Array 1, was located in the westernmost part of the dam area, close to the old seismic station STSW. It consisted of seven stations (ZEU107, ZEU108, ZEU109, ZEU110, ZEU127, ZEU128, ZEU130) with a triangular configuration (see Fig. 4). The inner four stations form the subarray 1b (ZEU107, ZEU127, ZEU128, ZEU130), which was a perfect equilateral triangle. The outer stations were, due to the site conditions, less regularly placed. The second array, Array 2, was formed by four stations (ZEU102, ZEU103, ZEU111, ZEU131) and located close to the final location of STSW2. The third array, Array 3, was formed on the rock to the east of Zeuzier Dam and consisted of four stations (ZEU202, ZEU203, ZEU206, ZEU222). The array recordings have been analyzed by the high-resolution 3-component FK algorithm (3C-HRFK; Poggi and Fäh, 2010) and by the modified SPAC algorithm (Aki, 1957; Bettig et al., 2001), implemented in the geopsy package.

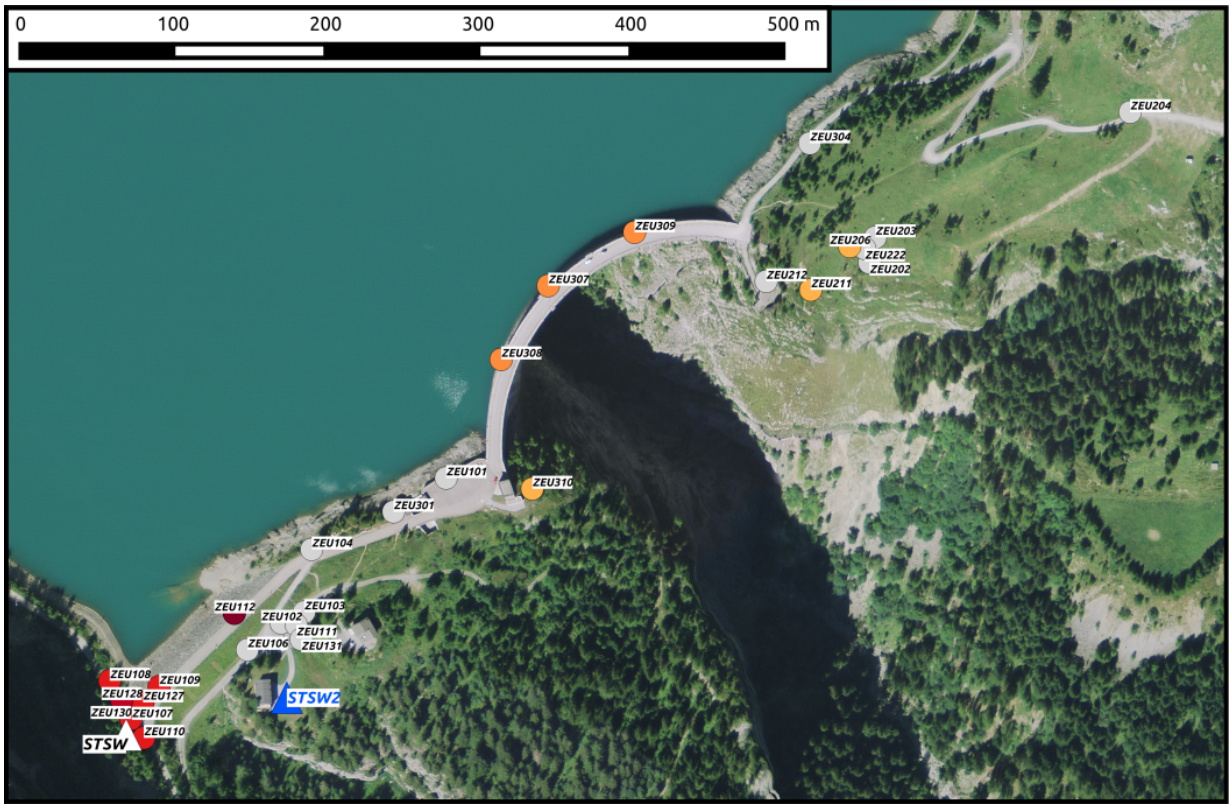

Figure 12: Map with the locations of the H/V measurements. Colored points correspond to points with a visible resonance frequency in the H/V curve, grey points have mainly flat H/V curves. The H/V curves for the different stations are shown in Figs 13-16.

5.1 Single-station analysis

The results of the single-station analysis are shown in Figs 13 - 18. The H/V curves are shown next to the polarization results for each station.
In the area around the old station STSW, where the geological map indicates debris, the H/V curves (Fig. 13) show peaks between 6 and 7 Hz. At station ZEU112, which was located on the artificial Proz-Riond Dam, a peak at 8.7 Hz is observed. The curves for all these stations are very similar, suggesting that the measurements to the west of the dam are affected by the eigenvibrations of the dam. The polarization for all stations on the debris show linear polarization mostly around the peak frequency, the polarized particle motion is in northwestern-southeastern direction, i.e. perpendicular to the Proz-Riond Dam. This would be in good agreement with the hypothesis that this dam has an eigenvibration in this frequency range, which is emitted to the southwest. Station ZEU112 on the eastern part of the dam, however, has a slightly higher resonance frequency and also shows a less pronounced polarization.
In the area between the Proz-Riond Dam and the Zeuzier Dam (Figs 14 and 15), the H/V curves have no apparent resonance peak and no prevalent polarization. This area is characterized by outcropping limestone. It is also in this area that station STSW2 is located. Station ZEU310 in the east has two small peaks at around 2 and 4 Hz. The 2 Hz peak corresponds to a linear polarization in north-south direction, the 4 Hz peak does not show a particular polarization pattern. The stations on the Zeuzier Dam (Fig. 16) show multiple peaks in the H/V curves and clearly linearized particle motion above 2 Hz, which is mainly orthogonal to the dam. This can be explained by a complex pattern of higher eigenmodes above the fundamental frequency of about 2 Hz. At station ZEU310, the radiation from the fundamental mode is observed and the 4 Hz peak might correspond to a surface structure at that place.
The stations to the east of Zeuzier Dam (Figs 17 and 18) show mainly flat H/V curves with only slight indications of peaks around 4 Hz (stations ZEU206 and ZEU222). No pronounced polarization can be observed there.

ZEU107

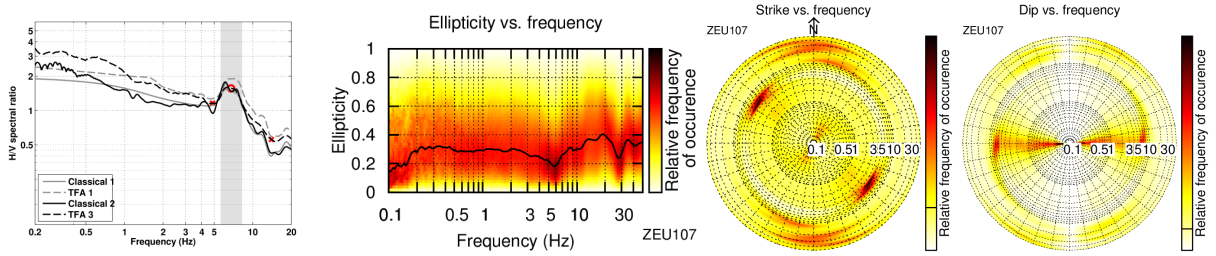

ZEU108

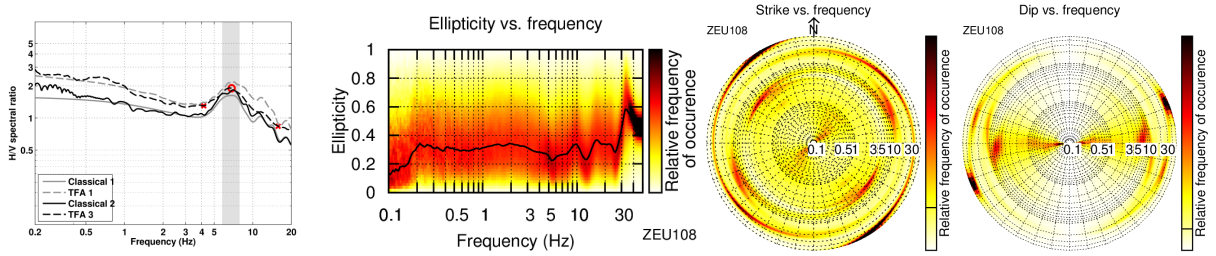

ZEU109

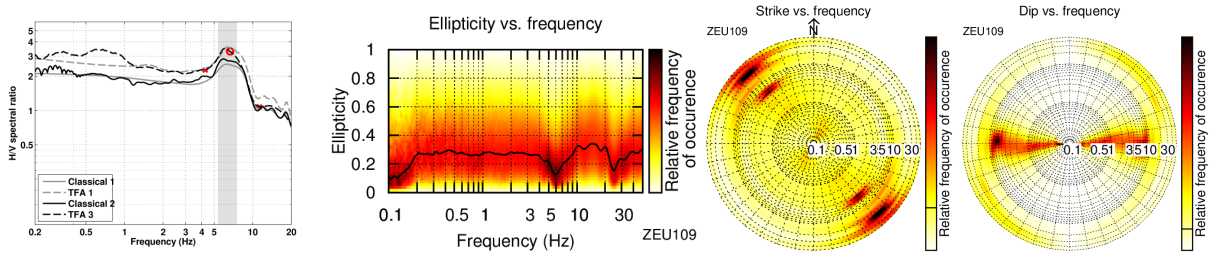

ZEU110

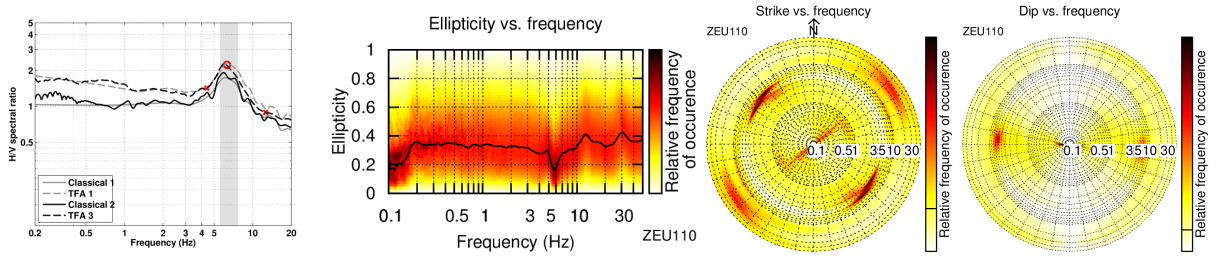

ZEU127

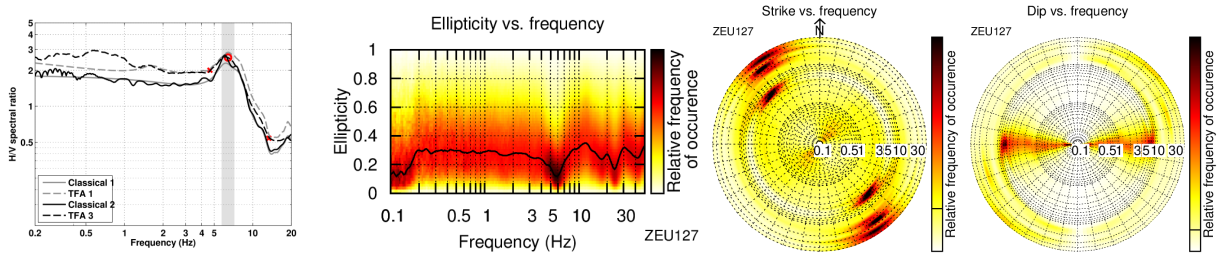

Figure 13: Left: H/V curves, as determined by different methods. Second to fourth columns: Polarization of the wave field, shown as ellipticity (second column, purely linear particle motion corresponds to 0, circular particle motion to 1), strike (third column, indicating the direction of polarization of the wave field) and dip (fourth column, indicating the dip of the polarization). The figure shows the results for the westernmost stations, close to the old station STSW.

ZEU128

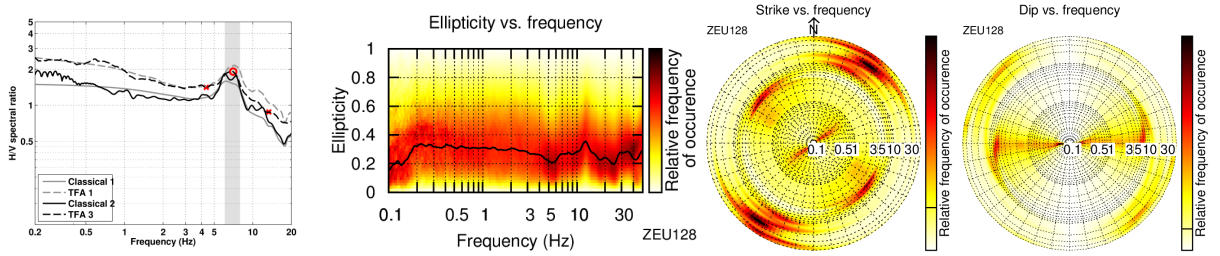

ZEU130

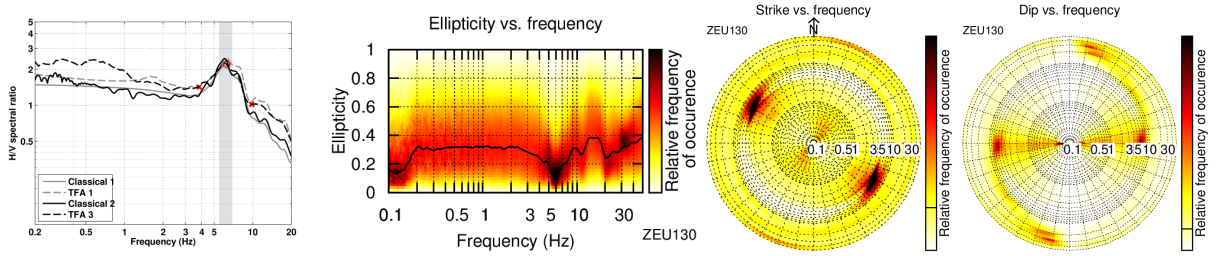

ZEU112

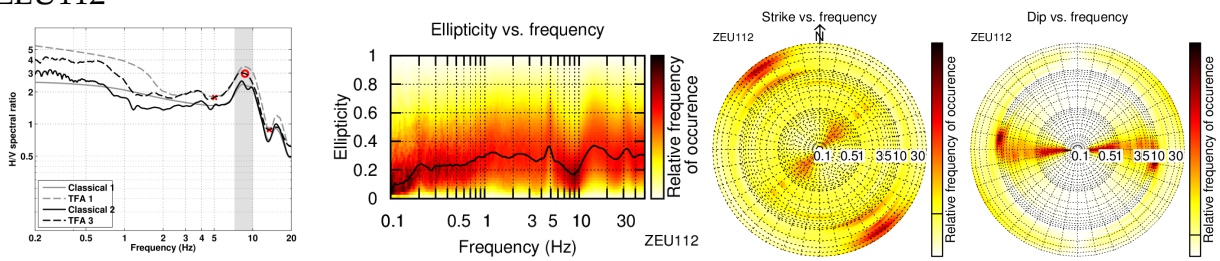

Figure 13: continued.

ZEU102

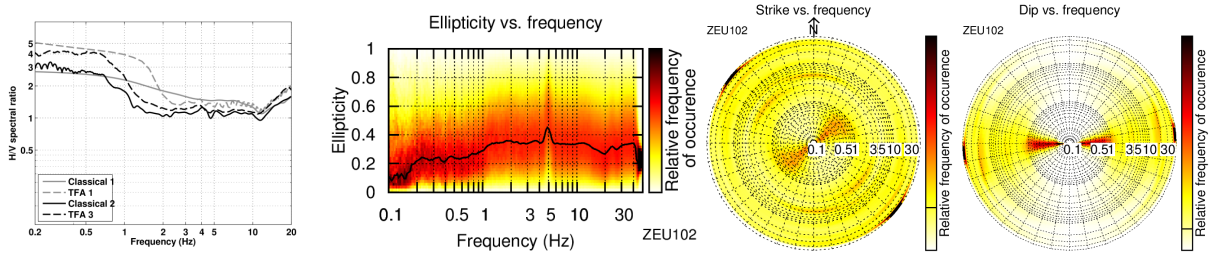

ZEU103

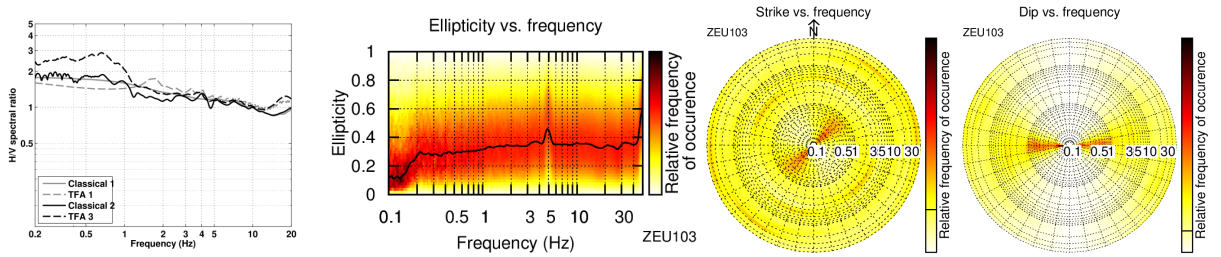

ZEU106

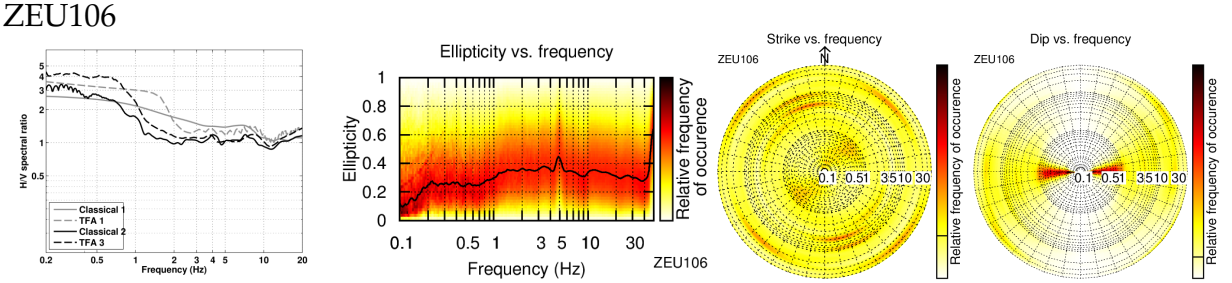

ZEU111

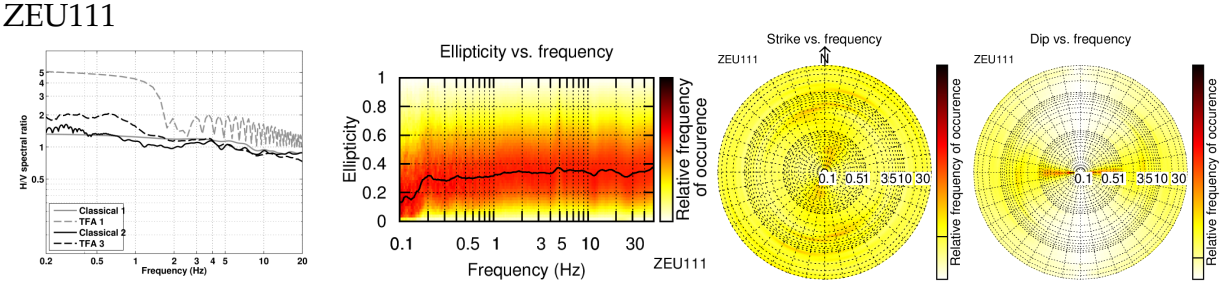

ZEU131

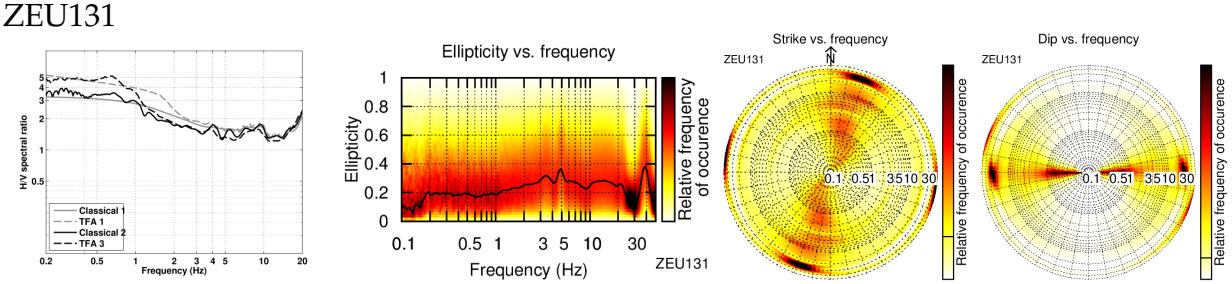

Figure 14: The same as Fig. 13, but for the stations closest to STSW2.

ZEU101

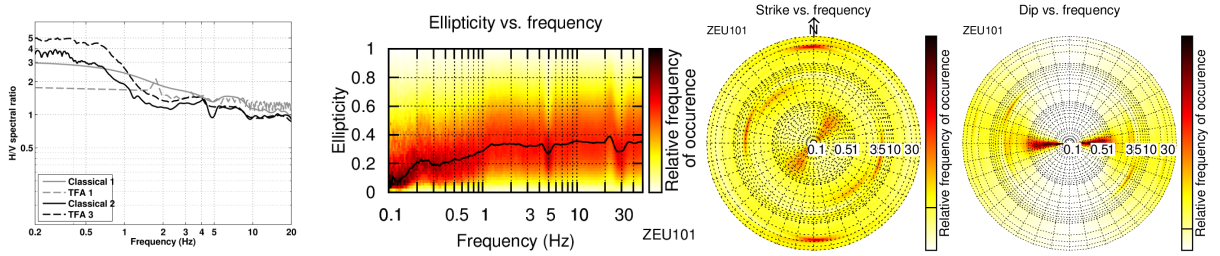

ZEU104

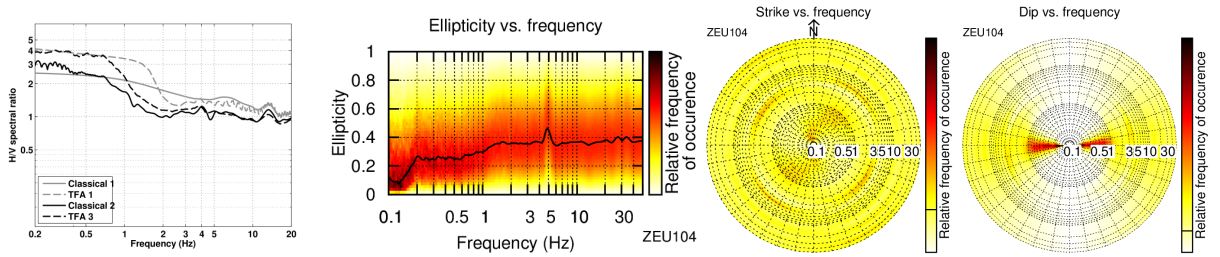

ZEU301

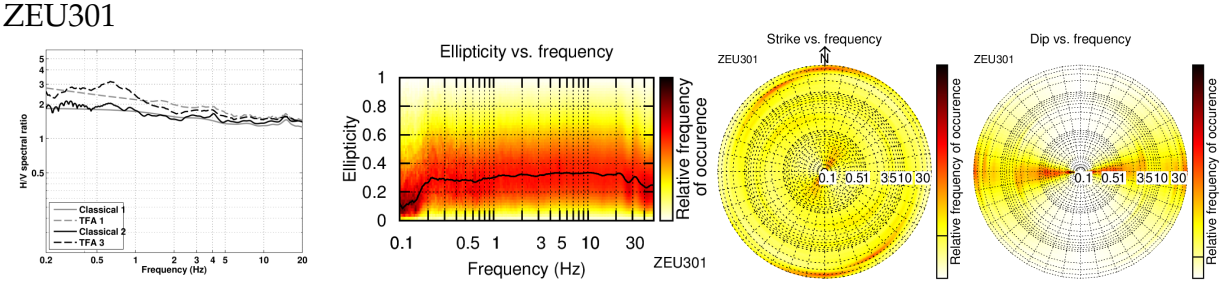

ZEU310

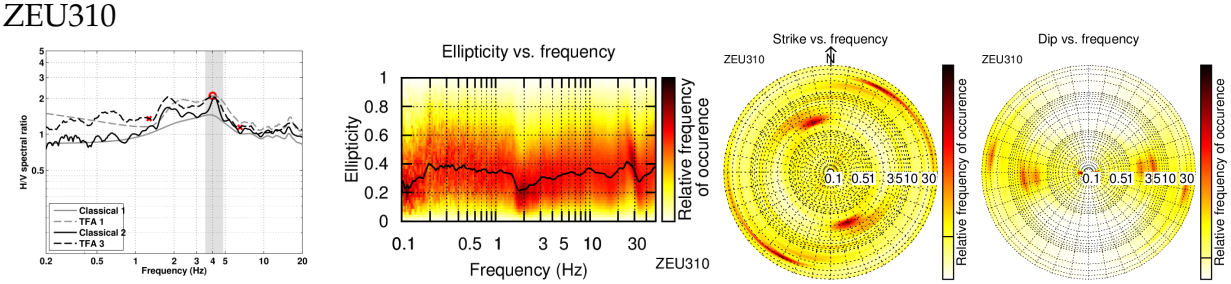

Figure 15: The same as Figs 13 and 14, but for the stations between the Proz-Riond Dam and the Zeuzier Dam.

ZEU307

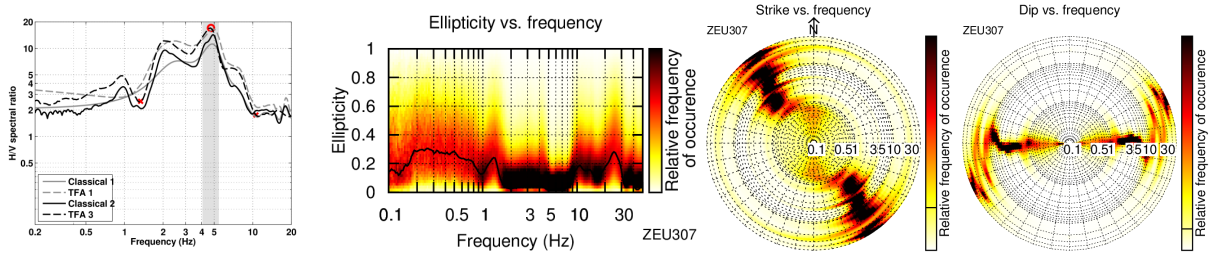

ZEU308

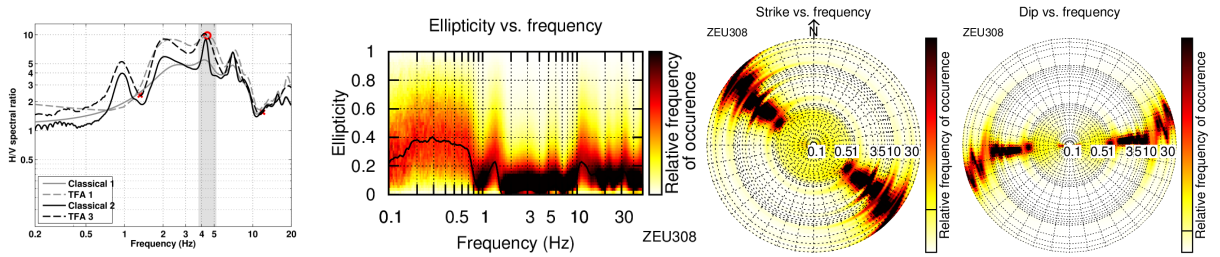

ZEU309

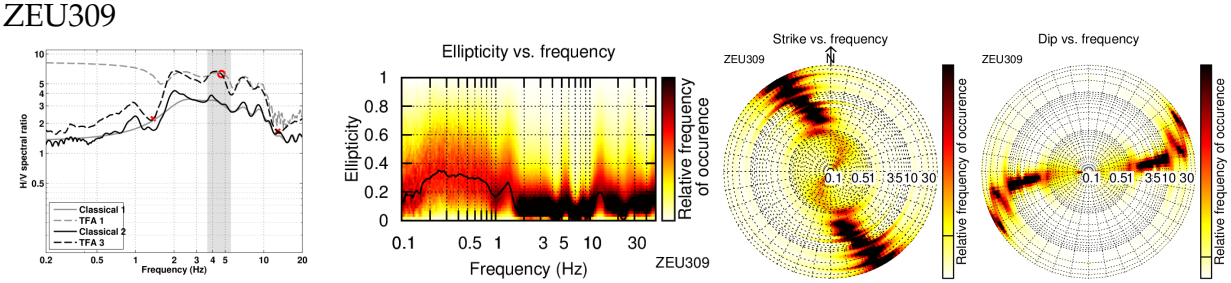

Figure 16: The same as Figs 13 - 15, but for the stations on the Zeuzier Dam.

ZEU202

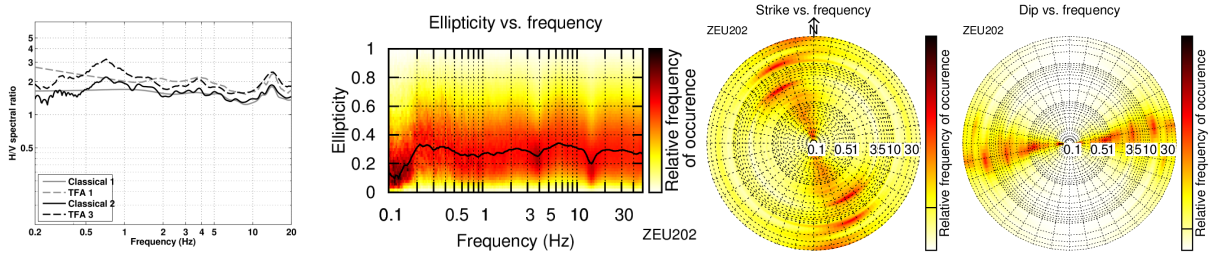

ZEU203

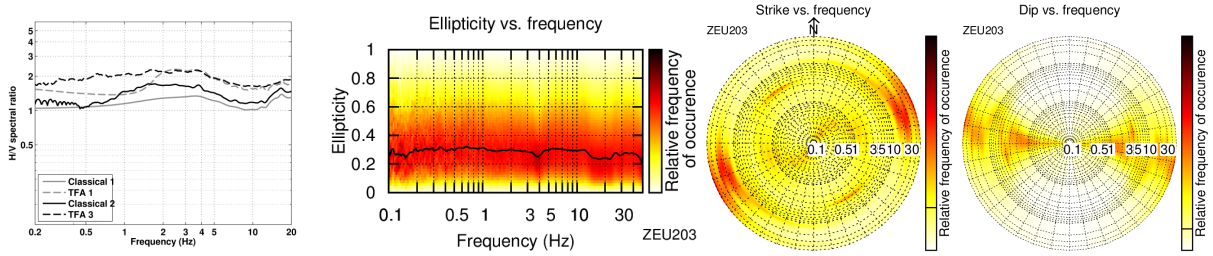

ZEU206

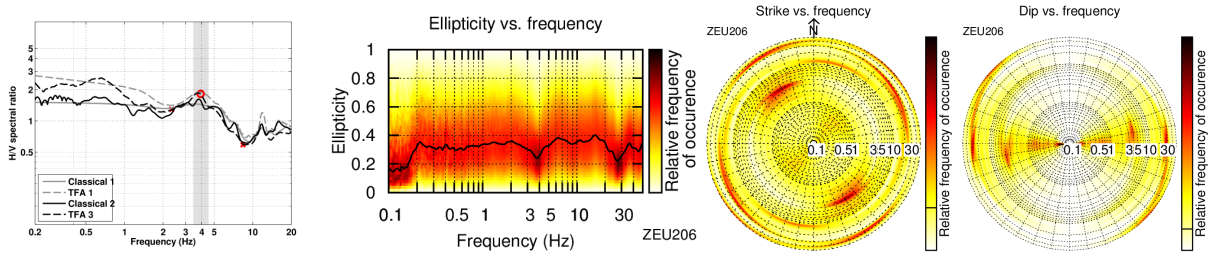

ZEU222

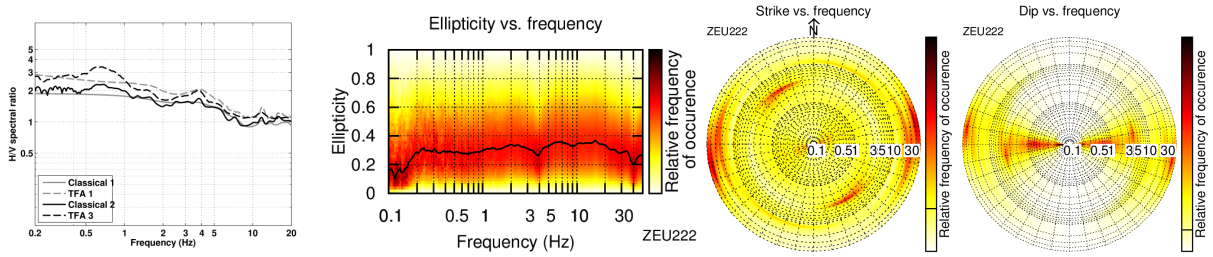

Figure 17: The same as Figs 13 - 16, but for the stations of Array 3 to the east of Zeuzier Dam.

ZEU204

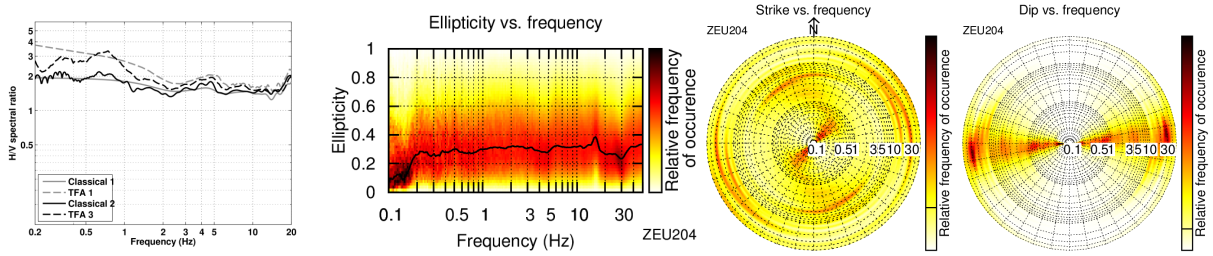

ZEU211

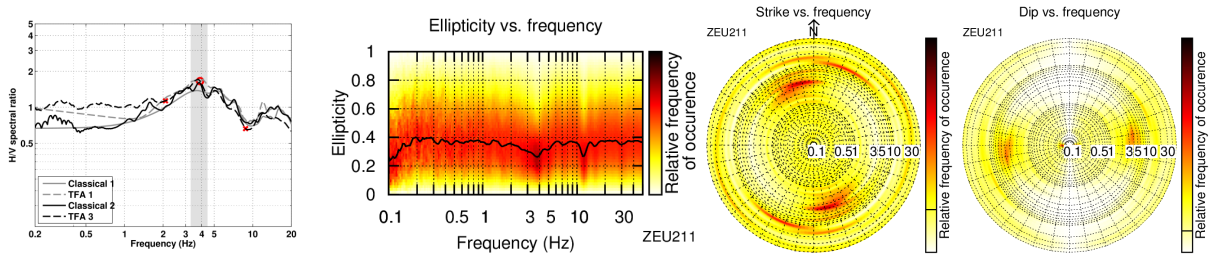

ZEU212

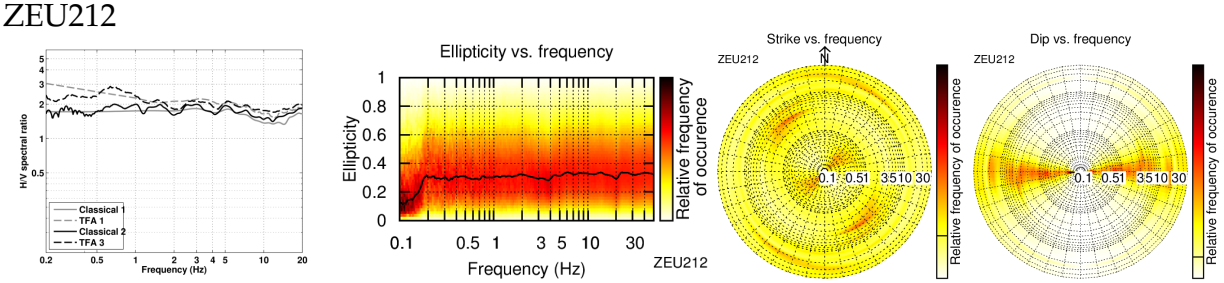

ZEU304

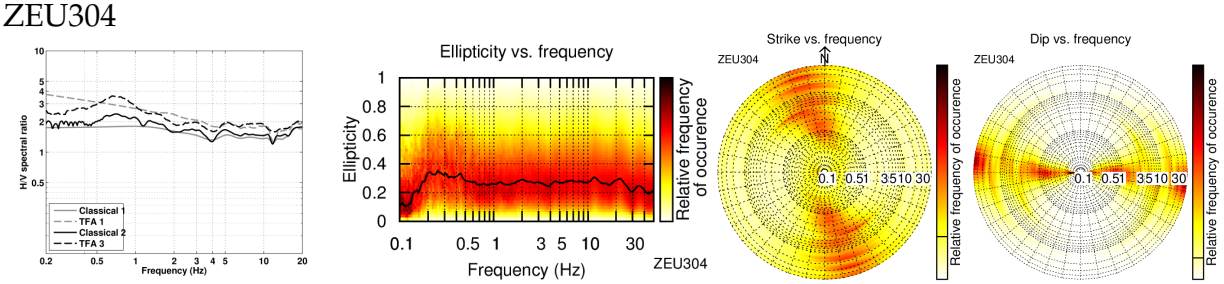

Figure 18: The same as Figs 13 - 17, but for the remaining stations to the east of Zeuzier Dam.

5.2 Array processing

The data of the small arrays 1, 1b, 2 and 3 were analyzed using the 3-component high-resolution frequency-wavenumber code (3C-HRFK; Poggi and Fäh, 2010). Furthermore, the vertical components of the recordings of these small arrays were analyzed using the modified SPAC method (Aki, 1957; Bettig et al., 2001). The array geometry of these small arrays was simple. Array 1b consists of four stations; a central station and three stations located on a circle of 8 m radius around the central station, where each pair of stations on the outer ring forms an angle of 120° as seen from the central station. For array 1, three additional stations were deployed in a distance of around 22 m, with deviations from the 120° angle due to local constraints. Arrays 2 and 3 consisted of four stations each, where three stations were set up at a distance of 10 m around the central station.

5.2.1 3C-HRFK

The 3C-HRFK analysis of array 1 (Fig. 19) yields a Rayleigh wave dispersion curve on the vertical component and a Love wave dispersion curve on the transverse component. The result on the radial component is too bad to identify a dispersion curve. For the vertical component, there is a strong line of maxima with increasing and decreasing velocities. Because of this questionable behavior, the other feature with smaller energy, following a more typical pattern, was picked as fundamental mode of the Rayleigh waves. For array 1b, the dispersion curve is retrieved in a smaller frequency range because of the limited resolution limits, but it is in quite good agreement with the larger array. Both dispersion curves are similar to the low-frequency dispersion curves determined using the MASW measurements (Fig. 10). The transverse dispersion curve, which we identify as a Love wave dispersion curve, is only visible in array 1. The ellipticity curves corresponding to the picked dispersion curves in arrays 1 and 1b (Fig. 19) are in good agreement and around 1.
For arrays 2 and 3 (Fig. 20), no dispersion curves can be identified on any component.

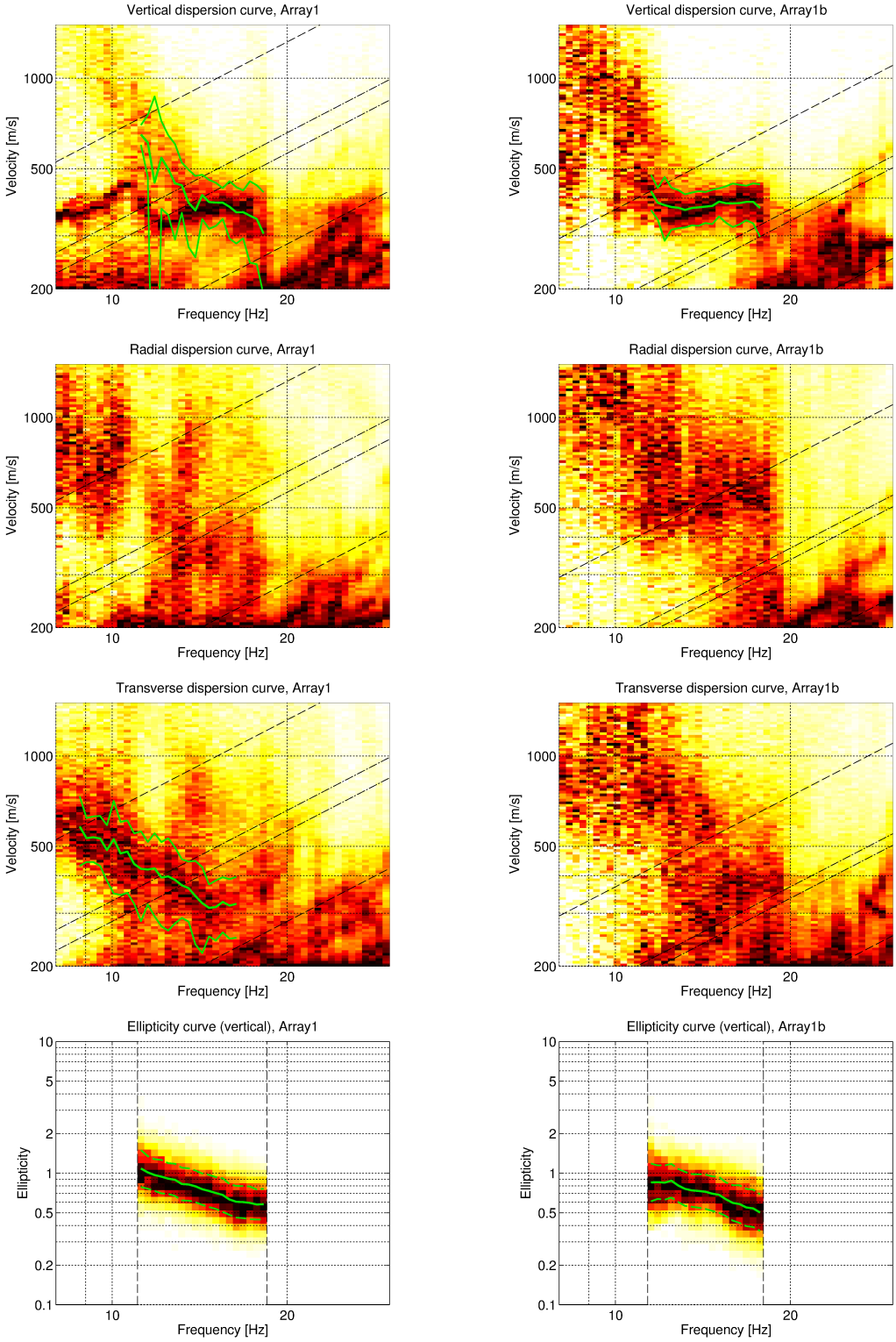

Figure 19: Dispersion and ellipticity curves obtained with the 3-component HRFK algorithm (Poggi and Fäh, 2010). In the left column, the results for array 1 are shown, in the right column for array 1b. From top to bottom the results for the vertical, radial and transverse components are shown. The dashed and dotted black lines are the array resolution limits. The solid green lines are picked from the data, where the central line indicates the best values and the two outer lines the standard deviation. The frequency ranges of the ellipticity curves correspond to the ranges where the corresponding dispersion curves had been picked.

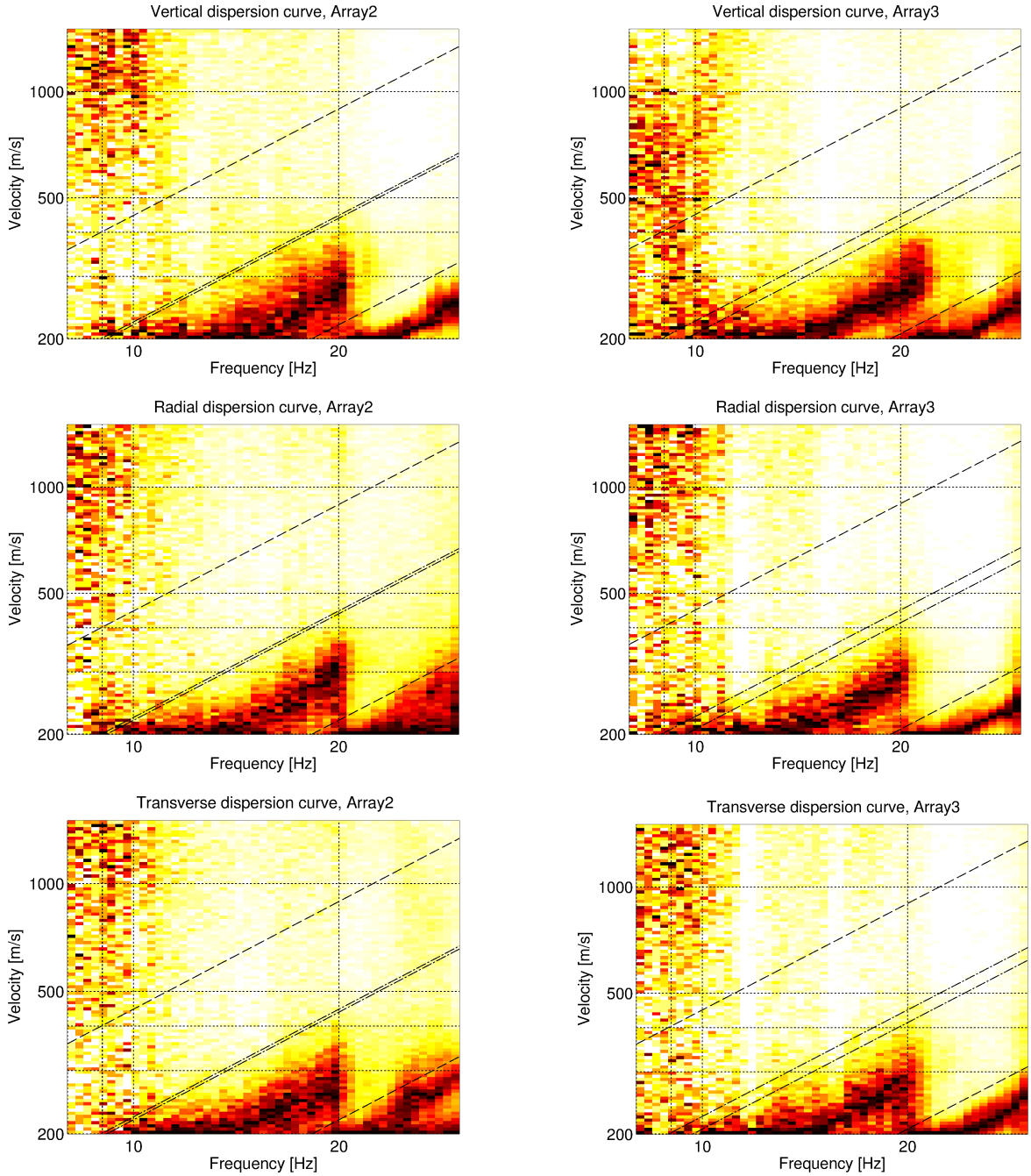

Figure 20: Results of the 3-component HRFK algorithm (Poggi and Fäh, 2010). In the left column, the results for array 2 are shown, in the right column for array 3. From top to bottom the results for the vertical, radial and transverse components are shown. The dashed and dotted black lines are the array resolution limits.

5.2.2 SPAC

For array 1, a total of six rings have been defined for which the SPAC curves have been calculated (Fig. 21). Only the two smallest rings yield SPAC curves that can be interpreted as the required Bessel functions. These two rings also belong to array 1b. When inverting the points which can be associated with the descending flank of the Bessel function, a Rayleigh wave dispersion curve can be retrieved between 11 and 17 Hz (Fig. 22), which is in agreement with the 3C-HRFK (Fig. 19) and the MASW measurements (Fig. 10). For array 2 and array 3, the resulting SPAC curves cannot be interpreted as Bessel functions (Fig. 23).

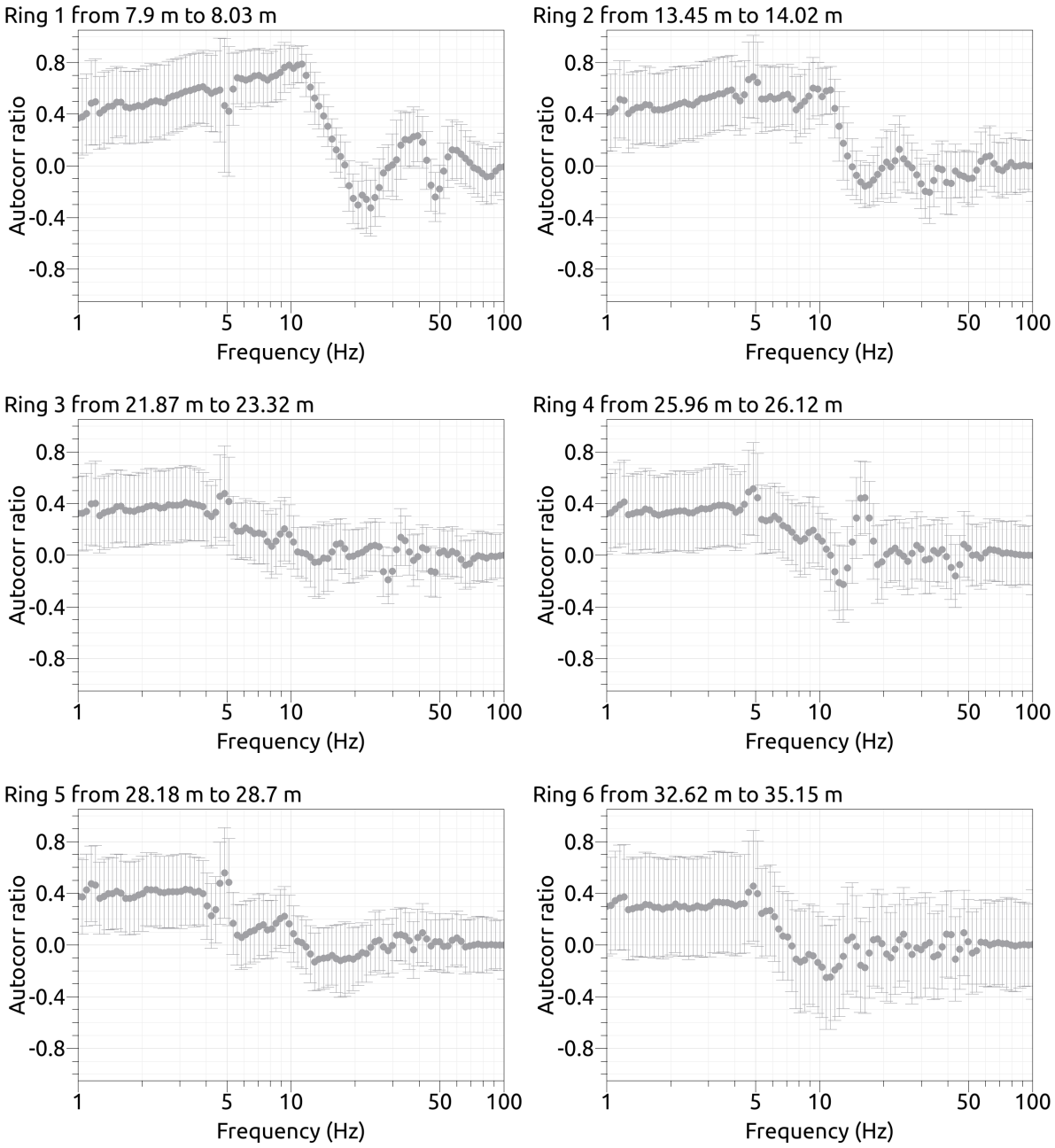

Figure 21: SPAC curves obtained for array 1.

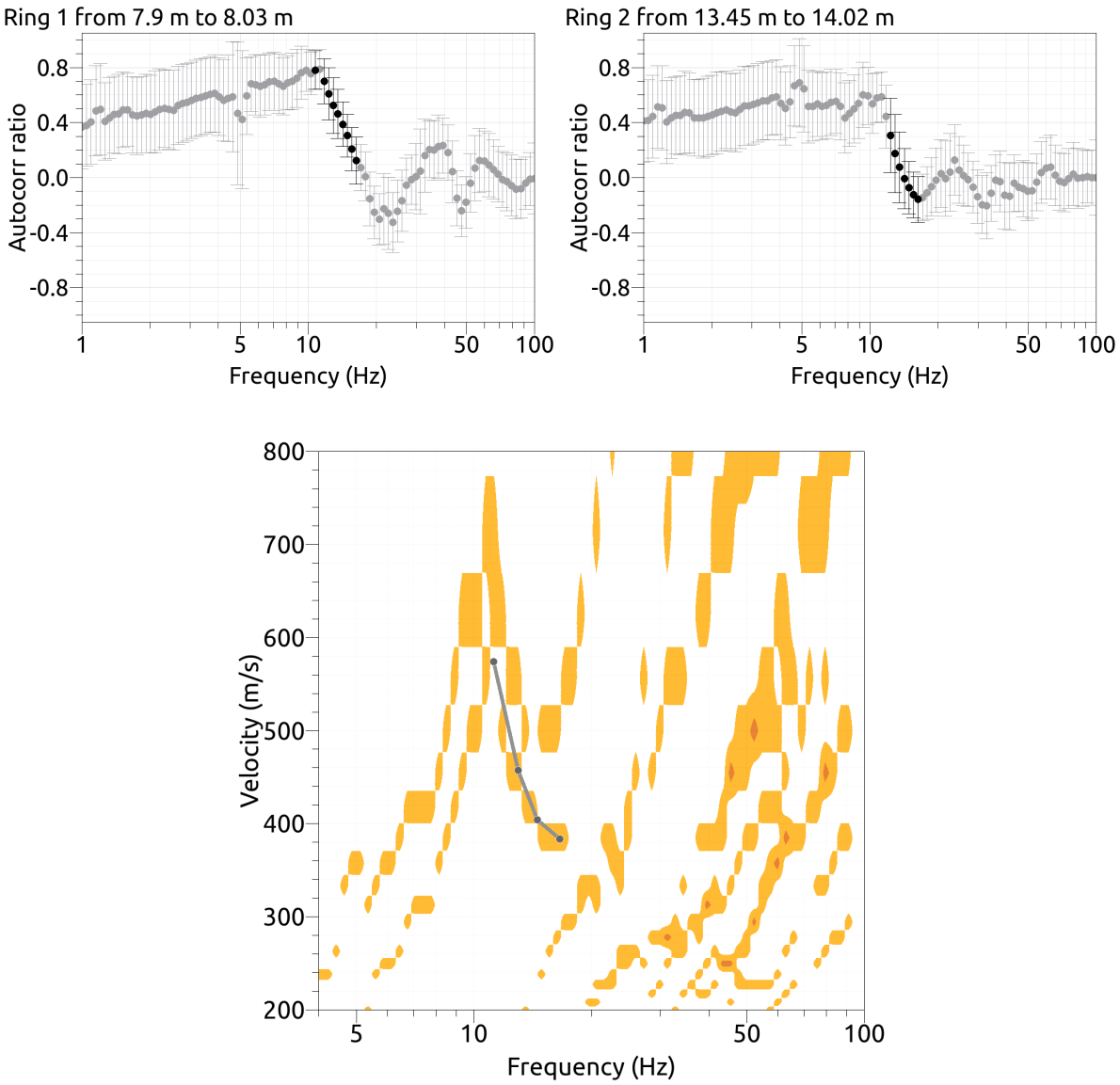

Figure 22: SPAC curves obtained for array 1b (top) and the picked dispersion curve obtained from the black points identified as part of the Bessel functions in these curves (bottom).

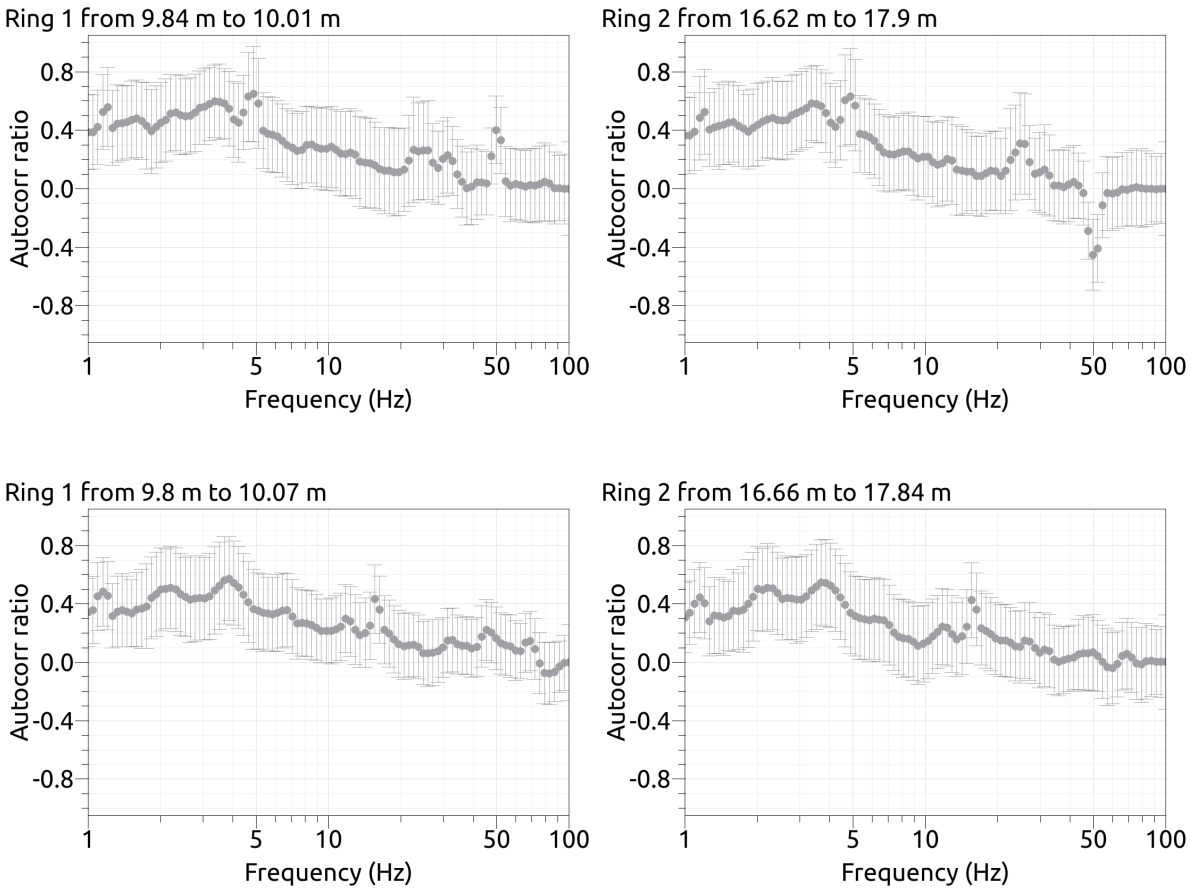

Figure 23: SPAC curves obtained for array 2 (top) and array 3 (bottom).

6 Inversion of the Rayleigh wave dispersion data

The Rayleigh wave dispersion curves obtained from the processing of MASW data were inverted to determine the seismic properties of the subsurface at the corresponding locations (Tseu1, Tseu2, Tseu3).
As explained in section 4.4.3, for each array four dispersion curves were obtained: one from the longitudinal component recordings and one from the vertical component traces, for both considered shooting locations (at both ends of the receiver spread; see Fig. 10). At each site, the four dispersion curves were merged into a single one through averaging: this global curve was hence fed to the inversion process.
Considering the difficulty in attributing the obtained data points to a given dispersion mode, we selected a Monte Carlo code (Maraschini and Foti, 2010) that does not require a priori mode numbering, but rather attempts itself to associate the input phase velocities to a defined Rayleigh wave mode, aiming at the best fitting solution that "explains" all (or most) of the picked dispersive events. The code implements a purely random search of the parameter space; its inversion procedure is divided into two steps. In the first stage, the misfit between each generated model and the experimental data is evaluated by computing the absolute value of the determinant of the Haskell-Thomson matrix at the phase velocity–frequency coordinates of the experimental curve points. Hence, no mode attribution is required, but the minimum misfit is achieved by the subsurface models for which the experimental points "fall" in the areas of the determinant surface that have absolute values close to 0 (i.e. close to modal curves). In the second inversion step, the code selects the model that performs best in the first stage, and accepts its corresponding mode attribution. Assuming this mode numbering, a second refinement run is performed, this time considering a classical Euclidean distance between experimental and synthetic curves as misfit function.
The same parameterization was used for the inversions of all three dispersion curves. The subsurface was modeled as a stack of 5 layers overlying a halfspace. For each layer, both thickness and velocity were let free to vary. As for seismic velocities, both the central value and the width of the Monte Carlo ranges increase layer by layer with depth. All three sites are known to be characterized by stiff soils or rock, hence the Poisson's ratio interval was set to 0.2 – 0.35 for all layers. The values of bulk density were attributed a priori to each layer, from 2000 kg/m^3 for the shallowest formation to 2700 kg/m^3 for the deepest one. For each site, 1.5 million randomly generated models were tested.

6.1 Inversion results

Fig. 24 shows the result of the first stage of the inversion procedure for the three sites: the experimental dispersion curve is superimposed to the absolute determinant surface of the best performing model. Most of the data points actually fall in the troughs of the surface, hence they are close to a particular modal curve, so that they are assigned to the corresponding mode for the second phase of the inversion. The phase velocity points that are found on the peaks of the determinant surface, i.e. without mode identification, were discarded. At all three sites, most of the phase velocities in the range $20 - 80\,Hz$ were attributed to the fundamental and first higher mode; at high frequencies (around $90 - 100\,Hz$) some data points align along a mode identified as the second higher mode. It is worth remarking that for Tseu2 and Tseu3 (both located on the rock formation) a mode jump from the fundamental to the first higher mode is observed (see also Fig. 25): this feature is known in literature to be proper of sites with shallow bedrock (Foti, 2002; Maraschini and Foti, 2010). As for Tseu3, it should be noted that the phase velocity points between 35 and 39 Hz are just beyond the lower-wavenumber array resolution limit and should therefore, rigorously, be discarded. Nevertheless, they belong to a clear dispersive branch extending across the resolution limit, identified as first higher mode, and they were hence retained.
Assuming this mode numbering, the final stage of the inversion was run, this time comparing the experimental dispersion curve with the modal curves from the Monte Carlo models. The 25 best performing models resulting from this refinement phase are shown in Figure 25; the corresponding synthetic curves are displayed in Fig. 24b.
The data fit between experimental and synthetic curves can be considered as satisfactory (Fig. 24b); however, the poor quality of the experimental curves causes a large variability among the retrieved feasible profiles. It is finally worth noticing that for Tseu2, the only site for which a credible V_P profile was obtained from refraction (4.4.2), both Rayleigh wave inversion and refraction identify the depth of the stiff layer beneath the soil cover at around 5 m.

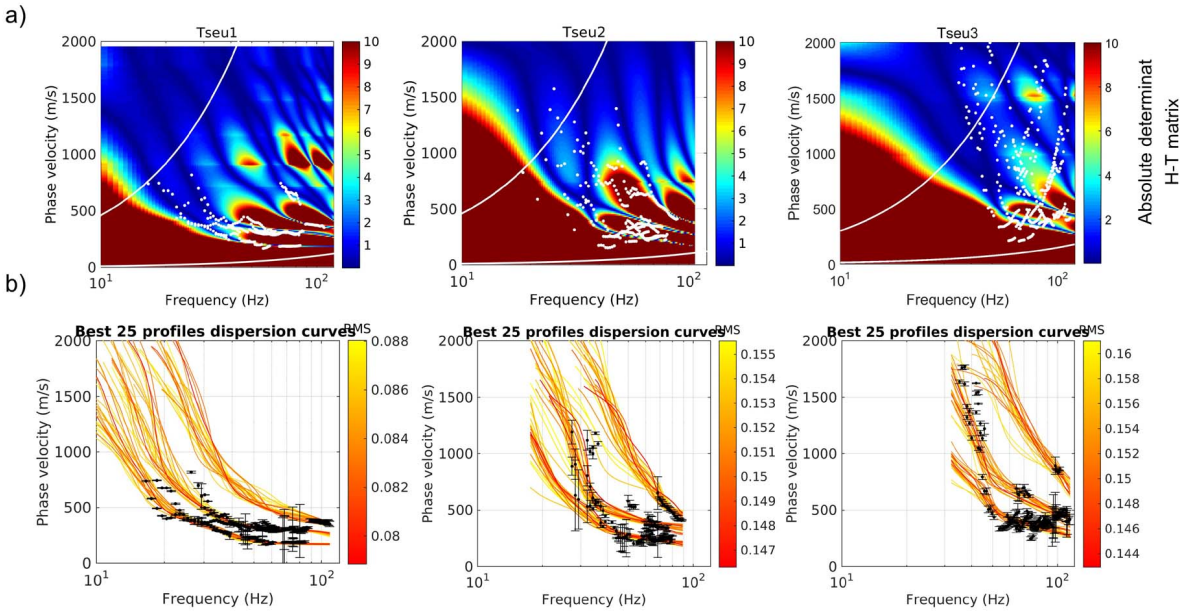

Figure 24: Experimental data fit in the two successive stages of the inversion procedure. a) Experimental dispersion curves (white dots) superimposed to the surface of the absolute determinant of the Haskell-Thomson matrix for the best performing model. b) Assuming the mode attribution proposed in (a), a refinement run is performed, considering a classical Euclidean distance between experimental and synthetic curves as misfit function.

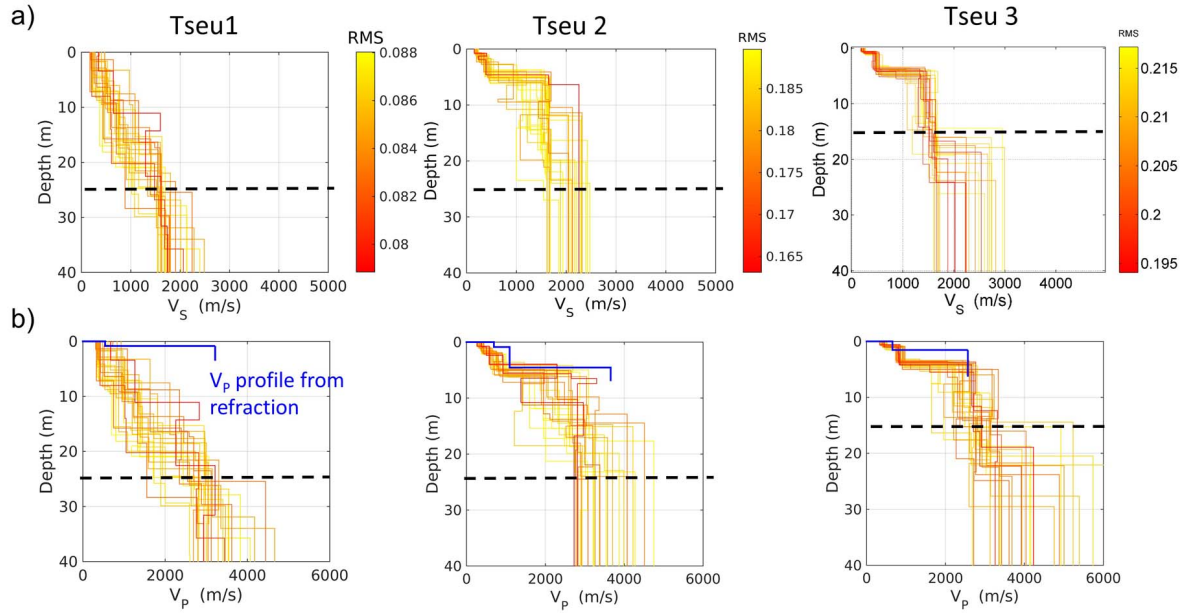

Figure 25: Inversion results: The 25 best performing subsurface models (out of a population of 1.5 million). Upper panels: V_S profiles. Lower panels: V_P profiles. The dashed black line marks the maximum depth of reliable investigation, which is assumed here as equivalent to the length of the receiver array.

6.2 Comparison with H/V curves

To reduce the large variability among the feasible profiles obtained from the dispersion curve inversion, we compared the peaks of the H/V curves from passive noise recordings with those of the SH transfer functions (Roesset, 1970) corresponding to the profiles provided by the Monte Carlo inversion. For this purpose, we selected for each site the passive station closest to the centre of the active array (stations ZEU110, ZEU 206 and ZEU310, respectively; distances ranging from 3.9 m for Tseu3 to 5.4 m for Tseu1).
The comparisons are displayed in Fig. 26. As for Tseu1, we focus on the fundamental frequency peak that clearly appears at 6 Hz in the H/V curves. Five subsurface models out of the 25 selected in the inversion process have a coinciding peak at approximately the same frequency (thicker SH transfer functions in Fig. 26a). The corresponding velocity profiles (Fig. 26b) reduce the variability of the feasible models provided by the Monte Carlo inversion; they identify a velocity contrast at approximately 20 m depth, most likely between the upper layer of debris deposit ($V_S \approx 550\,m/s$, in accordance with the geological information for Tseu1) and the underlying formation that can be interpreted as composed of weathered rock ($V_S \approx 1500\,m/s$; the same value is identified also for Tseu2 and Tseu3 at shallower depths).
The H/V curves at Tseu2 show a clear peak at 28 Hz, but the SH transfer functions of the best models show a peak at 20 Hz. It might be that the underground between the H/V point and the active seismic line changes, especially the thickness of the surficial layer. Actually, the measurement is at a gentle slope, so small-scale differences in the underground are not surprising. These models place the interface between surficial soil cover ($V_S = 420\,m/s$) and weathered rock ($V_S \approx 1500\,m/s$) at 5.4 m depth: this impedance contrast is responsible for the peak at 20 Hz. Changing this interface to lower depth, around 4 m, would explain the 28 Hz from the H/V measurement. At larger depths, at around 22 m, fractured rock is replaced by a more compact formation ($V_S \approx 2000 - 2500\,m/s$).
Similar considerations can be drawn for Tseu3. Here again the fundamental peak is quite low, 4.0 Hz, so we focus our attention on two higher peaks (at 16 and 32 Hz). Three out of 25 models present similar features (Fig. 26a). The corresponding V_S profiles have two clear interfaces: at 4.5 m depth, between surficial soil cover ($V_S = 530\,m/s$) and weathered rock ($V_S \approx 1500\,m/s$; this interface can be related to the 32 Hz peak) and at 21 to 24 m, this time between weathered and compacted rock below ($V_S = 2200 - 2800\,m/s$; this interface can be related to the 16 Hz peak). It should be noted that this latter interface is deeper than the investigation depth rigorously allowed by the used array (15 m). Nevertheless, considering its consistency with H/V data, and its similarity with the other two profiles (particularly in terms of estimated velocities), we anyhow assume this reconstruction plausible.

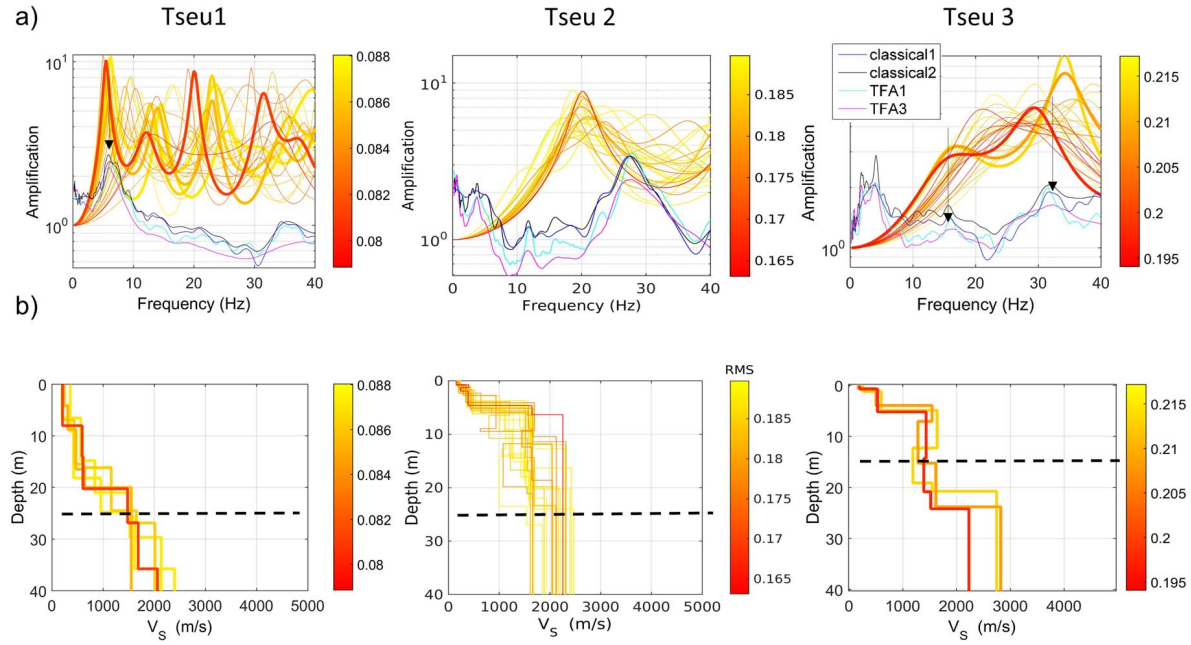

Figure 26: a) Comparison between the SH transfer functions of the 25 best subsurface models from the Monte Carlo inversion (shaded color lines) with the H/V curves from the closest passive noise recording station (black, blue, cyan and magenta lines). The SH transfer functions that present peaks considered in agreement with those from the H/V curves are represented with thicker lines. The black arrows highlight the correlation. b) V_S profiles corresponding to the thicker SH transfer functions in (a).

7 Quarter wavelength representation

The quarter-wavelength velocity representation (Joyner et al., 1981) attributes to each frequency the average velocity at a depth equal to a quarter of the corresponding wavelength (Fig. 27). It can also be considered as a proxy in estimating the depth of reliable investigation of the available experimental data. In the presented sites, the minimum acceptable frequencies for the phase velocity curves are indeed relatively high (16 Hz for Tseu1, 23 Hz for Tseu2 and 35 Hz for Tseu3), as these frequencies are constrained by the limited extent of the corresponding arrays. In a quarter-wavelength representation, these frequency intervals correspond to qwl-depths of few meters. However, higher modes were included in the inversion procedure at all three sites (Fig. 24b): as several literature works have highlighted (Xia et al., 2003; Ernst, 2008), these should allow greater investigation depths.
The estimated V_{S30} are 490, 942 and 1138 m/s for Tseu1, Tseu2 and Tseu3, respectively (Fig. 27). In terms of soil classification, according to Eurocode 8 (CEN, 2004), Tseu1 is at the border between soil classes B and E: three out of the five accepted profiles (Fig. 26b, left panel) satisfy the definition of soil class E ($V_{S30} < 360\,m/s$ until 20 m depth, underlain by stiffer layers with $V_S > 800\,m/s$). The other two models have V_{S30} for the layers overlying the bedrock slightly larger than 360 m/s (369 and 389 m/s, respectively), hence they should be classified as soil type B. When considering SIA261 (SIA261, 2014), however, all feasible profiles are class E without ambiguities. Tseu3 and Tseu2 are class A soils ($V_{S30} > 800\,m/s$) both for Eurocode 8 and SIA261.

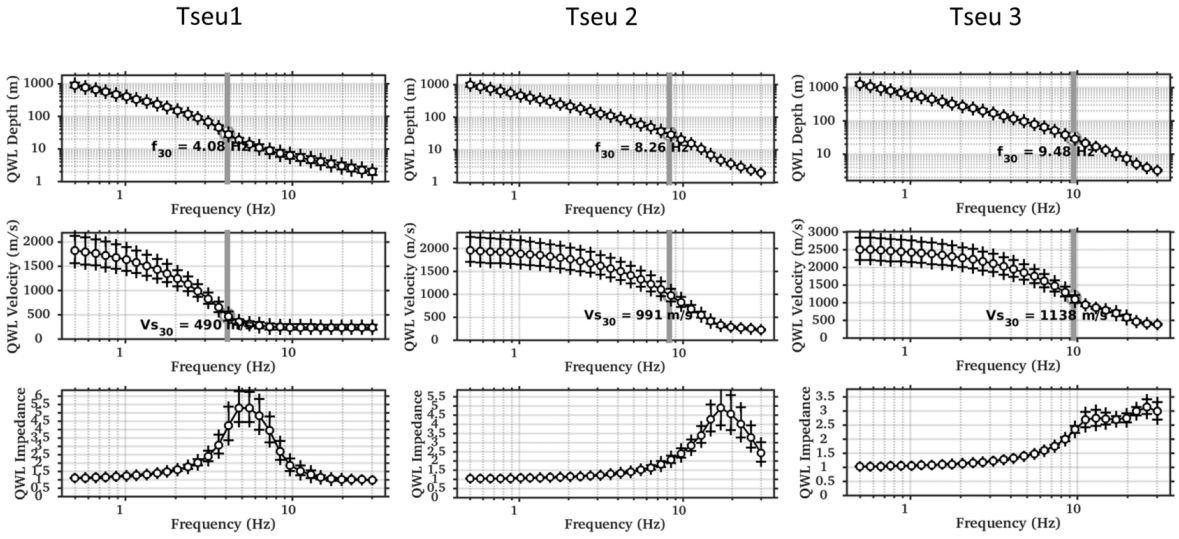

Figure 27: Quarter-wavelength representation of the selected velocity profiles (Fig. 26). Top: depth; center: velocity; bottom: impedance contrast. The gray line in the top and center panel refers to V_{S30}.

8 SH transfer functions

The average theoretical SH-wave transfer functions for vertical propagation (Roesset, 1970) were computed over the selected models for all three sites (Fig. 28). The transfer functions were corrected for the Swiss reference rock model (Poggi et al., 2011), following Edwards et al. (2013). These are compared with the empirical amplification function obtained by empirical spectral modeling (ESM; Edwards et al., 2013; Michel et al., 2014). No particular similarity or correlation can be identified between the empirical and the simulated transfer functions. This can be explained with the fact that STSW2 was installed in a location that is relatively far from the three sites for which velocity profiles were estimated: in the following section an attempt to infer information regarding the subsurface beneath STSW2 is presented.

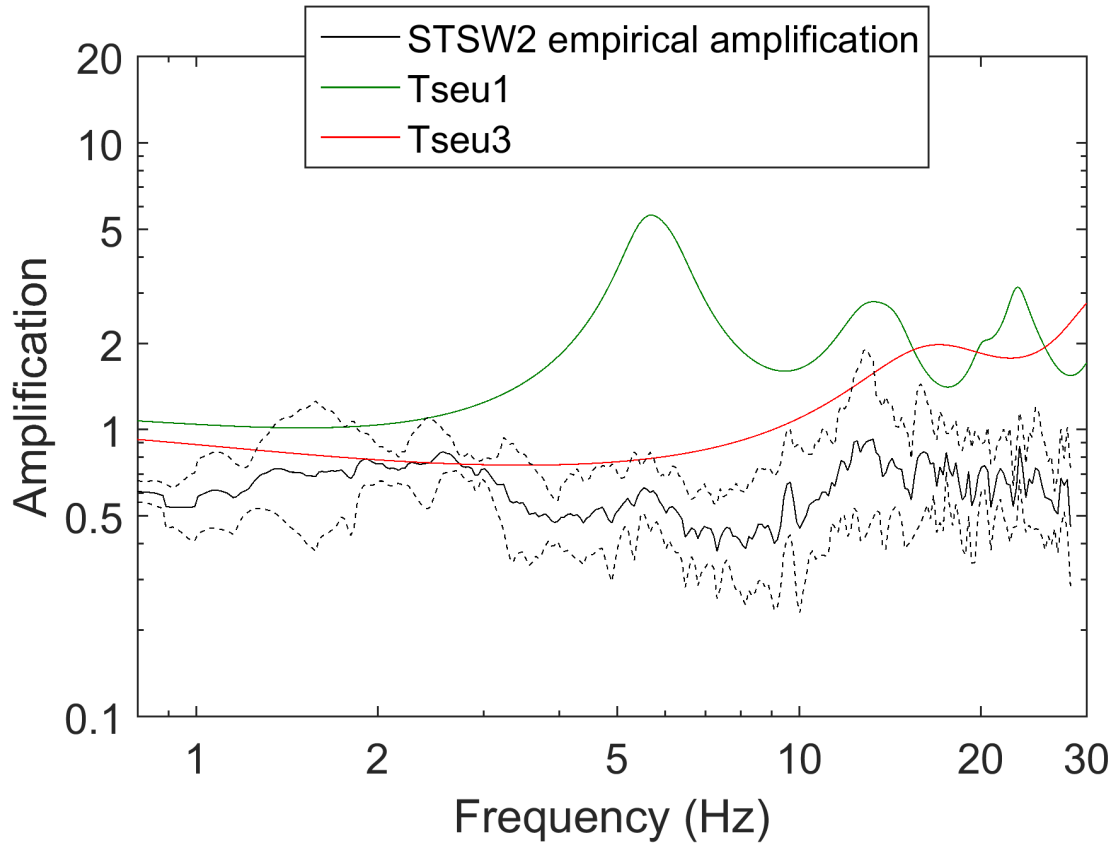

Figure 28: Empirical amplification function from STSW2 recordings (black line) compared with the average SH transfer functions (referred to the Swiss bedrock) from the estimated profiles for Tseu1 and Tseu3.

9 Deduction of the structure beneath station STSW2

As described earlier, the site characterization measurements presented in this report were carried out before the installation of STSW2 and helped in defining the final site for the station. The final location of STSW2 was chosen on the outcropping rock between the Proz-Riond and the Zeuzier Dams. This location represents a site with low noise ratio, the eigenvibrations of both the Proz-Riond Dam and the Zeuzier Dam do not influence the recording.
Unfortunately, all active seismic lines are relatively far from the position of STSW2; the comparison between the empirical amplification functions from STSW2 and the simulated SH transfer functions from sites Tseu1, Tseu2 and Tseu3 shows that none of the estimated velocity models can directly describe the subsurface beneath the SSMNet station. This is also confirmed in Fig. 29, where the empirical amplification function for STSW2 is compared with the ellipticity curves from single-station noise recordings closest to the active seismic lines (also used in 6.2): no similarity on the distribution of the peaks between the empirical function and the ellipticity curves can be observed.
This applies also to the ellipticity curve (magenta line in Fig. 29) from the single station recording closest to STSW2 (station ZEU106 about 38 m north-north-west of STSW2). Hence, also this curve could not be used to draw any information regarding the subsurface model at STSW2.
The strategy that was considered to approximate the velocity profiles at the station location was to adjust the models estimated from active surveys, taking into account the geomorphology of the site and aiming at a resemblance between empirical and simulated transfer function. Tseu1, placed on a surficial layer of debris sediments, was discarded from this inference process; in fact, STSW2 is directly located on the rock formation, as Tseu2 and Tseu3. Therefore, Tseu3 has the closest compatible velocity profile, and was selected for the subsoil property estimation at STSW2.
Fig. 30 shows the comparison between the empirical amplification function for STSW2 and the synthetic SH transfer functions (referenced to the Swiss bedrock) from the three acceptable profiles obtained for Tseu3 (thinner lines, same colors as Fig. 25b). As already observed in section 6.2, these are characterized by a peak at 16 Hz, which should correspond to the interface between degraded and compact rock formations. The empirical amplification function at STSW2 shows instead a peak at 13 Hz; this could indicate a larger depth for the weathered/fresh rock boundary. This interpretation is compatible with the geomorphology of the site: STSW2 is in fact located on a spur extruding from the rocky ridge marking the south-east shore of the lake, its south and west walls showing exposed rock (Fig. 2). Hence it is reasonable to expect a thicker layer of degraded rock (extending along the height of the spur) between the surficial soil cover and the compact bedrock below.
The thickness of the intermediate layers modeling the degraded rock (between 4.5 and 21 - 24 m depth, $V_S \approx 1500\,m/s$ in Fig. 25b, right panel) was therefore increased by 10 % steps: the best fit with the 13 Hz peak is achieved with an increment of 40 % (see thicker lines in Fig. 30). This means that the interface between weathered rock layers ($V_S \approx 1500\,m/s$) and fresh bedrock below ($V_S = 2200 - 2800\,m/s$) would be moved from 21 – 24 m to a depth range of 27 – 32 m. According to these estimated profiles, the soil classification for STSW2 should correspond to site class A, for both Eurocode 8 (CEN, 2004) and SIA261 (SIA261, 2014).

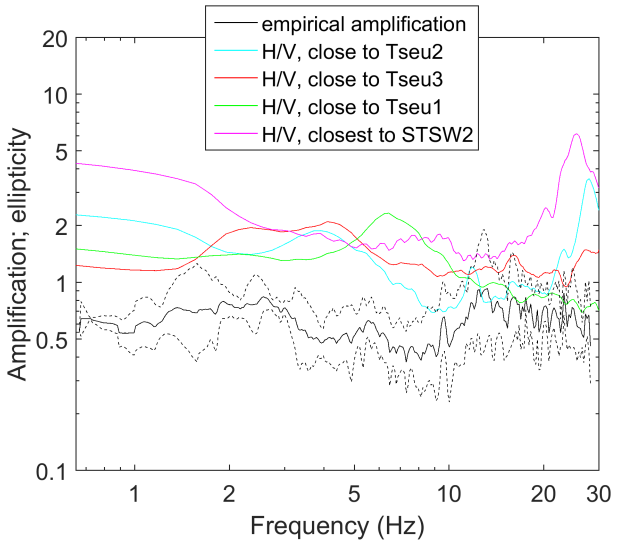

Figure 29: Empirical amplification function from STSW2 recordings (black line) compared with the ellipticity curves from the three single station recording in proximity of the active lines (cyan, red, green lines), and with the ellipticity curve from the noise recording closest to STSW2 (magenta line).

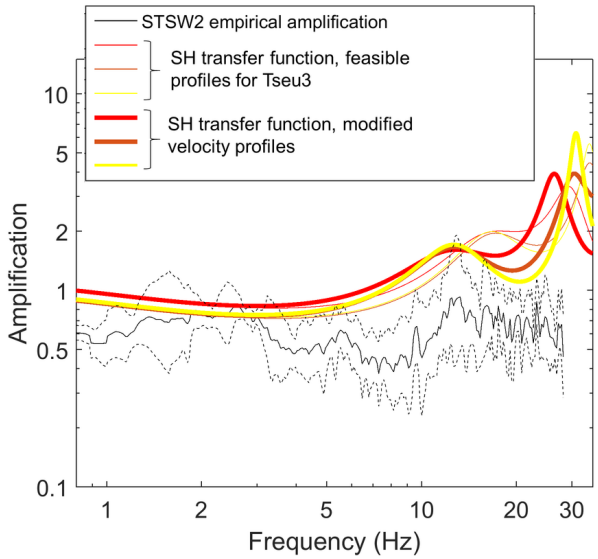

Figure 30: Empirical amplification function for STSW2 (black line) compared with the synthetic SH transfer functions (referenced to the Swiss bedrock) computed for the feasible profiles obtained for Tseu3 (thinner colored lines). These velocity profiles were modified increasing the thickness of the intermediate formations (depths between 4.5 m and 21 - 24 m, $V_S \approx 1500\, m/s$ in Fig. 25b), modeling weathered rock. The best agreement with the empirical function was obtained when increasing the thickness of said layers by 40 % (thicker colored lines).

10 Conclusion

This reports presents the results obtained from a site characterization survey carried out in proximity of station STSW2, prior to its installation. Active seismic measurements along three lines and a series of single-station noise recording measurements were performed. Passive data were processed to derive local H/V and ellipticity curves. Active acquisitions were processed with MASW and P-wave refraction techniques to estimate the velocity profiles within the shallow subsurface; these were also compared with noise recording results.

The investigated site is a rocky ridge (limestone) bordering one side of a reservoir lake in the mountains of the right flank of the Rhone Valley (VS). The south-west shoulder of the ridge is covered by debris sediments. Two active seismic lines were deployed on the emerging rock formation; the corresponding velocity profiles show about 5 m of surficial soil cover ($V_S = 200 - 530\,m/s$, increasing with depth) overlying a formation composed of 3 layers with $V_S \approx 1500\,m/s$, with overall thickness around 20 m, which should correspond to weathered rock. The interface between fractured and compact rock below ($V_S = 2000 - 2800\,m/s$) should then be located at a depth of 20 to 24 m. The soil at the locations of these seismic lines is class A for both Eurocode 8 and SIA261. The interface between the soil cover and the fractured rock about 5 m depth and the boundary between weathered and fresh rock about 22 m correspond to peaks at 23 - 32 Hz and around 16 Hz in the H/V curves derived from the single station recordings acquired on the rock formation. These are also characterized by fundamental peaks at much lower frequencies (around 4 Hz), that can be explained with an interface within the rock formation, at larger depths than those surveyed by active acquisitions.

The third active line was placed on the area covered by debris. The obtained velocity profiles place the interface between the shallower sediments ($V_S = 210 - 610\,m/s$, increasing with depth) and what can be interpreted as weathered rock (again $V_S \approx 1500\,m/s$), at a depth of around 20 m. This boundary can be correlated with the fundamental frequency peaks ($6 - 8\,Hz$) observed in the H/V curves from single station recordings performed in the debris fan area. As for this third location, the five feasible models drawn from the inversion of the Rayleigh wave dispersion curve can be all classified as soil class E when considering SIA261; according to Eurocode 8, two profiles belong to class B (V_{S30} for the sediments is slightly larger than the 360 m/s limit prescribed for E soils), while the other three remain in class E.

Unfortunately, neither the MASW lines nor the single station noise recordings were actually placed at the location later chosen for the installation of station STSW2. As a consequence, it is only possible to propose an estimation of the subsurface structure beneath STSW2. The velocity profiles obtained from the closest compatible MASW line were adjusted to match the empirical amplification function obtained for STSW2. The resulting subsoil models have about 5 m of surficial soil cover, overlying 22 – 27 m of degraded rock, in turn resting on a compact rock layer further below. This hypothesis is compatible with the geomorphology of the location selected for the SSMNet station.

Acknowledgements

The authors thank Oona Brunner and Dylan Longridge for their help during the array measurements.

References

Aki, K. (1957). Space and time spectra of stationary stochastic waves, with special reference to microtremors. *Bull. Earthquake Res. Inst. Tokyo Univ.*, 35:415–456.

Bettig, B., Bard, P.-Y., Scherbaum, F., Riepl, J., Cotton, F., Cornou, C., and Hatzfeld, D. (2001). Analysis of dense array noise measurements using the modified spatial auto-correlation method (SPAC): application to the Grenoble area. *Boll. Geof. Teor. Appl.*, 42:281–304.

Boiero, D. and Socco, L. V. (2010). Retrieving lateral variations from surface wave dispersion curves analysis. *Geophysical Prospecting*, 58:977–996.

Burjánek, J., Gassner-Stamm, G., Poggi, V., Moore, J. R., and Fäh, D. (2010). Ambient vibration analysis of an unstable mountain slope. *Geophys. J. Int.*, 180:820–828.

Burjánek, J., Moore, J. R., Molina, F. X. Y., and Fäh, D. (2012). Instrumental evidence of normal mode rock slope vibration. *Geophys. J. Int.*, 188:559–569.

CEN (2004). Eurocode 8: Design of structures for earthquake resistance - Part 1: General rules, seismic actions and rules for buildings. Technical report, European Committee for standardization (CEN), Brussels, Belgium.

Edwards, B., Michel, C., Poggi, V., and Fäh, D. (2013). Determination of site amplification from regional seismicity: Application to the swiss national seismic networks. *Seismological Research Letters*, 84:611–621.

Ernst, F. (2008). Multi-mode inversion for p-wave velocity and thick near-surface layers. In *Proceedings of the Near Surface 2008 14th European Meeting of Environmental and Engineering Geophysics, Krakow, Poland*.

Foti, S. (2002). Numerical and experimental comparison between 2-station and multistation methods for spectral analysis of surface waves. *RIG (Italian Geotech. J.)*, 36:11–22.

Foti, S., Lai, C. G., Rix, G. J., and Strobbia, C. (2015). *Surface Wave Methods for Near-Surface Site Characterization*. CRC Press, Taylor & Francis Group LLC.

Joyner, W. B., Warrick, R. E., and Fumal, T. E. (1981). The effect of quaternary alluvium on strong ground motion in the coyote lake, california, earthquake of 1979. *Bull. Seismol. Soc. Am.*, 71:1333–1349.

Maranò, S., Hobiger, M., and Fäh, D. (2017). Analysis of rayleigh waves with circular wavefront: a maximum likelihood approach. *Geophys. J. Int.* under review.

Maraschini, M. and Foti, S. (2010). A monte carlo multimodal inversion of surface waves. *Geophys. J. Int.*, 182:1552–1566.

Michel, C., Edwards, B., Poggi, V., Burjánek, J., Roten, D., Cauzzi, C., and Fäh, D. (2014). Assessment of site effects in alpine regions through systematic site characterization of seismic stations. *Bull. Seismol. Soc. Am.*, 104:–.

Park, C. B., Miller, R. D., and Xia, J. (1999). Multichannel analysis of surface waves. *Geophysics*, 64:800–808.

Poggi, V., Edwards, B., and Fäh, D. (2011). Derivation of a reference shear-wave velocity model from empirical site amplification. *Bull. Seismol. Soc. Am.*, 101:258–274.

Poggi, V. and Fäh, D. (2010). Estimating Rayleigh wave particle motion from three-component array analysis of ambient vibrations. *Geophys. J. Int.*, 180:251–267.

Redpath, B. B. (1973). Seismic refraction exploration for engineering site investigations. Technical Report E-73-4, National Technical Information Service.

Reynolds, J. M. (2011). *An introduction to applied and environmental geophysics*. John Wiley & Sons, Ltd.

Roesset, J. (1970). Fundamentals of soil amplification. In Hansem, R. J., editor, *Seismic Design for Nuclear Power Plants*, pages 183–244. MIT Press, Cambridge, Mass.

SIA261 (2014). Einwirkungen auf tragwerke. Technical report, SIA (Schweizerischer Ingenieur- und Architektenverein), Zurich, Switzerland.

Socco, L. V., Boiero, D., Foti, S., and Wisen, R. (2009). Laterally constrained inversion of ground roll from seismic reflection records. *Geophysics*, 74:G35–G45.

Socco, L. V. and Strobbia, C. (2004). Surface-wave method for near-surface characterization: a tutorial. *Near Surface Geophysics*, 2:165–185.

Xia, J., Miller, R. D., Park, C. B., and Tian, G. (2003). Inversion of high frequency surface waves with fundamental and higher modes. *J. Appl. Geophys.*, 52:45–57.